Pontificia Universidad Católica del Perú

Escuela de posgrado

Comparison and evaluation of measured and simulated High-Frequency Capacitance-Voltage curves of MOS structures for different interface passivation parameters

A thesis submitted for the degree of Master of Science (M. Sc.) in Physics

Presented by:
Miguel Ángel Sevillano Bendezú

Supervisor:
Dr. Jan Amaru Palomino Töfflinger

Committee:

Dr. Jorge Andrés Guerra Torres
Dr. Rolf Grieseler

February 2019

Το ψυχή

Abstract

Semiconductor-insulator interfaces play an important role in the performance of many different electronic and optoelectronic devices such as transistors, LEDs, lasers and solar cells. Particularly, the recombination of photo-generated charge carriers at interfaces in crystalline silicon solar cells causes a dramatic efficiency reduction. Therefore, during the fabrication process, the crystalline silicon must be subjected to prior superficial passivation; typically through an insulating layer such as SiO_2, SiN_x or AlO_x. The function of this passivating layer is to reduce electrical recombination losses in interfacial defect states originating from dangling bonds. The associated passivation parameters are, on the one hand, stable charges within the insulating layer (Q_{ox}) that by repelling a certain type of charge carrier from the crystalline silicon surface, reduces its recombination effectiveness (Field Effect Passivation). On the other hand, the density of surface defect states or the interface trap density (D_{it}), which is reduced by the passivation layer (Chemical Passivation). These passivation parameters (Q_{ox} and D_{it}) turn out to be relevant when evaluating the effectiveness of a new material with passivating properties, as well as relevant for different theoretical models that allow simulations of the spectral response and/or efficiency in solar cells under different passivation conditions. One of the techniques widely used for studying the interfacial passivation properties of semiconductor electronic devices is the extraction of these interfacial passivation parameters through of capacitance-voltage (C-V) measurements on metal-oxide-semiconductor (MOS) or metal-insulator-semiconductor (MIS) systems.

In the present work, a simulation tool for High-Frequency C-V curves based on simulated Q_{ox} and the D_{it} was developed using Python. As a first step, the simulation was developed for an ideal MOS system, i.e. for $Q_{ox} = 0$ and $D_{it} = 0$. A verification of the resulting, simulated band-bending was reached through a band diagram simulator (The *Multi-Dielectric Band-Diagram* program).

As a second step, the program was subjected to an evaluation and validation through experimental data. This data comprises measurements of C-V and their respective extracted parameters for a sample of silicon dioxide thermally grown on crystalline silicon wafer (SiO_2/c-Si). Using three different models for the D_{it} distribution within the band gap energy: Gaussian model, U-shape model, and a constant value, approximations of the corresponding experimental C-V curve were obtained. It was evident that the C-V curve simulated from the D_{it} based on the model with Gaussian distributions for the defect centers and exponentials for the band tails resulted in the best approximation of the experimental C-V curve. It should be noted that the other two models were adjusted based on the value of the D_{it} near to midgap energy, where the recombination probability and rate are the highest. In this way, the constant model of the D_{it} at the midgap presented the largest deviation in the simulated C-V curve among the used models.

An implicit fitting method of the D_{it} through the experimental C-V curve fitting is proposed. For this, the U-shape model is used because it only depends on three parameters. The average values of the fitted and the experimentally extracted D_{it} are compared.

The parameter D_{it}^0, which defines the value at midgap in the U-shape model could be interpreted as an average estimation of the D_{it} energetic range values around the midgap where recombinations are most significant. Therefore, this parameter could determine a representative value of the D_{it}.

Finally, the developed program allows an in-depth analysis of the passivation parameters from which the surface passivation is evaluated.

Resumen

La interfaz entre un semiconductor y un aislante juega un papel importante en el desempeño de diferentes dispositivos electrónicos y optoelectrónicos, tales como transistores, LEDs, láseres y celdas solares. Una de las técnicas ampliamente empleadas en el estudio de las propiedades interfaciales de dispositivos electrónicos semiconductores es la extración de parametros interfaciales por medio del modelo de un sistema Metal-óxido o aislante-semiconductor (MOS o MIS) sobre medidas de Capacitancia en función del voltaje (C-V). Uno de estos dispositivos, en el cual se encuentra una fuerte aplicabilidad debido al interés de investigación son las celdas solares de alta eficiencia basadas en silicio cristalino, las cuales, en la mayoría de los casos deben ser sometidas a una previa pasivación superficial del material absorbente (comunmente silicio cristalino), por medio de una capa pasivadora, aislante (como el SiO_2, SiN_x o AlO_x). La función de esta capa pasivadora es la de reducir las pérdidas eléctricas por recombinación en defectos interfaciales. Los parametros asociados son por un lado, cargas estables dentro la capa aislante (Q_{ox}) que al repeler un cierto tipo de la superficie del silicio cristalino, reduce su efectividad de recombinación (pasivación por efecto de campo) y por lo lado, la reducción de la densidad de estados superficiales D_{it} del semiconductor (pasivación química). Estos parámetros de pasivación (Q_{ox} y D_{it}) resultan ser relevantes al momento de evaluar la efectividad de un nuevo material con propiedades pasivadoras, así como también son relevantes para los distintos modelos teóricos que permiten hacer simulaciones de la respuesta espectral y/o de la eficiencia en celdas solares bajo distintas condiciones. Es conocido que como primera aproximación la representación de una D_{it} por medio de un único estado resulta ser un buen punto de partida para estos modelos así como también una forma práctica de comparación de la pasivación química para distintas capas pasivadoras.

En el presente trabajo se desarrolló, mediante el lenguaje Python, una herramienta de simulación de curvas C-V medidas a alta frecuencia en base a Q_{ox} y D_{it} simulados.

Inicialmente la simulación es desarrollada para un sistema MOS ideal para diferentes conjuntos de ecuaciones, una solución exacta y otra aproximada del modelo usado, encontrándose una buena estimación de ambas curvas simuladas. En un primer instante un parámetro principal (*band-bending potential*) del programa, a partir del cual se construyen las curvas C-V, es validado con un simulador de diagrama de bandas (*Multi-Dielectric Band-Diagram*) obteniéndose un buen ajuste para el *band-bending potential*.

Como segunda medida el programa fue sometido a una evaluación y validación por medio de datos experimentales. Estos datos comprenden medidas de C-V y sus respectivos parámetros extraidos para una muestra de óxido de silicio crecido térmicamente sobre obleas de silicio cristalino (SiO_2/c-Si). Usando tres diferentes modelos, modelo gausiano, modelo U-*shape* y de valor constante, para simular la D_{it}. A partir de estos modelos se obtuvieron aproximaciones de la curva C-V experimental. Además comparando los distintos modelos se evidenció que el modelo gausiano es el más aproximado. Cabe señalar que los otros dos modelos se ajustaron en base al valor de la D_{it} en la mitad del ancho de banda (valor energético dónde más efectiva es la recombinación) el cual es conocido como *midgap*. De este modo, el modelo constante de D_{it} en el midgap presenta el mayor error entre los tres modelos usados.

Un método de ajuste implícito de la D_{it} a través del ajuste de la curva C-V experimental es planteado. Para ello el model U-*shape* es usado debido a que solo depende de tres parámetros. Los valores promedios de la D_{it} ajustada y experimentalmente extraída son comparados, obteniéndose una aproximación hasta la segunda cifra significativa.

Se da una supuesta interpretación de uno de los parámetros asociados a este modelo U-shape, el valor constante que define el midgap y sus alrededores, como el promedio de los valores centrales de la D_{it} experimental, cuya recombinación es significativa respecto al valor en el *midgap*. Por lo tanto este parámetro hallado podría determinar una D_{it} representativa a la hora de comparar diferentes curvas de D_{it}.

Finalmente el programa desarrollado podría permitir un análisis profundo de los parámetros de pasivación a partir de los cuales la pasivación superficial es evaluada.

List of Figures

List of Tables

Contents

Chapter 1

Introduction

1.1 General introduction

Semiconductor interfaces are a relevant part of the present challenges at the ecosystem of the electronics industry nowadays (figure 1.1). From Ultra Large Scale Integration (ULSI) technology, to emerging technologies [Dev18]. Device density [Int17], low energy consumption [Nin19], reduction in production cost, among others are some important topics in which disruptive innovation in semiconductor devices is involved [Anw17].

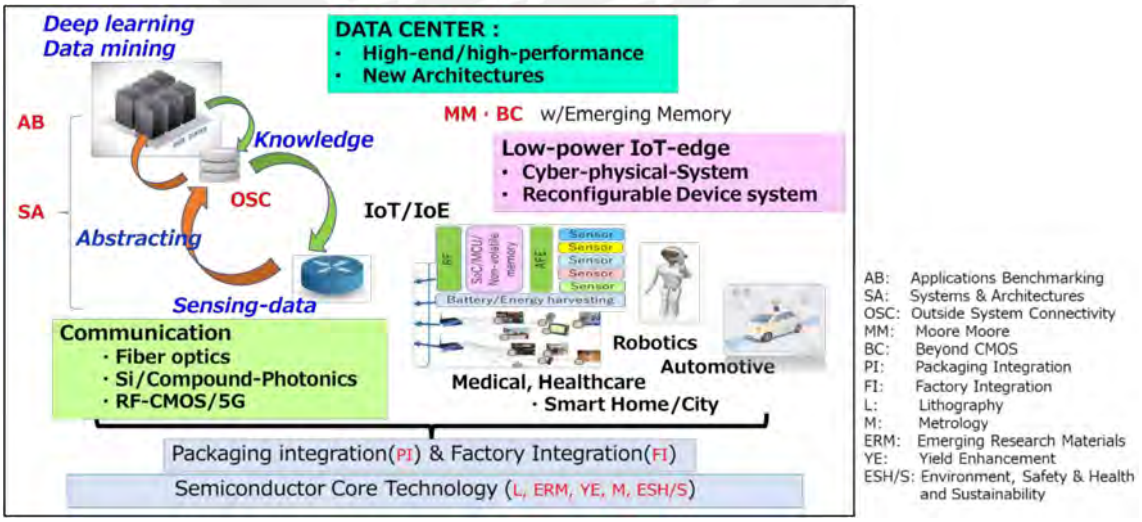

Figure 1.1: The New Ecosystem of the Electronics' Industry based on Semiconductor Technologies from the International Roadmap for Devices and Systems [Dev18]

.

Thus, in the photovoltaic industry, the semiconductor interfaces are crucial to con-

sider for the high efficiency solar cells. For example, the highest laboratory-type solar cell based on silicon [Yos17; Gre19] have interfaces which were exhaustively passivated, thus, reaching a maximum conversion efficiency of 26.7 %, which is very close to the theoretical limit for silicon (29 %) predicted by A. Richter et al. [Ric13]. The fundamental efficiency limit of a solar cell based on a single semiconductor absorber is called the *Shockley-Queisser theoretical limit* [Sho61] and depends principally on the semiconductor band gap (see figure 1.2).

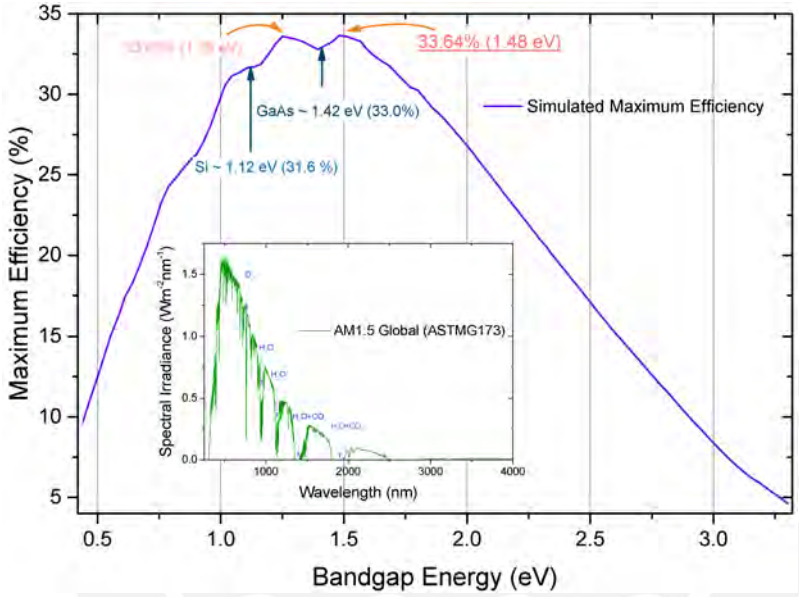

Figure 1.2: The Shockley-Queisser limit for real data: AM1.5G spectrum simulated using Python based on the S. Byrnes's code [Byr16]

In this sense, recombination of photo-generated charge carriers through interface defect states [Bon17] is one of the most limiting factors in comparison with other losses in a solar cell (see figure 1.3) [Glu07].

Therefore, novel passivation materials are continually being investigated in order to have better optical properties along with better passivation properties trying, in turn, to maintain or reduce the production cost of solar cells as much as possible [Mäc02; Din12; Kru14; Cue15; Bla16; Bon17]. Several experimental techniques are used in order to evaluate such capabilities.

Investigations based on metal-oxide (insulator)-semiconductor, MOS systems, have given significant results in the semiconductor interface field due to their ease of fabrication in comparison to other devices. This is thanks to W. H. Brattain, J.L. Moll, R. Lindner, E. H. Nicollian, A. S. Grove, and many other semiconductor specialists who laid the foundations of this field.

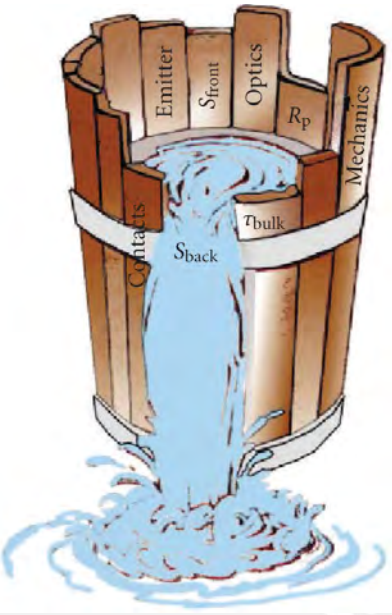

Figure 1.3: Liebig's law adapted to solar cells [Glu07]. The parameters losses and cell components in this figure are depicted. Effective surface recombination velocity S_{back} represents the most limiting loss parameter among all losses.

At present, MOS simulations based on physical models (classical or quantum mechanical) allow to deeply investigate the interfacial phenomena related to novel materials in MOS systems. Despite that many simulation tools are already available to the community [Ric01; Mat14], very few allow to introduce experimentally extracted passivation parameters, such as D_{it} and Q_{ox} in order to perform a deeper investigation and analysis of these materials. This work is focused on the development of a tool to simulate the passivation-dependent C-V characteristic of MOS systems and its results are shown in the following chapters.

1.2 Surface Recombination

Surface defect states at the beginning were part of an hypothetical conception in a theoretical work about the termination of the lattice and dangling bonds on the surface of a crystalline material suggested by Igor Tamm in 1932 [Tam32]. In the following years, many other researchers did theoretical contributions using different abstractions [Sho39] with the aim to obtain the most general and sophisticated abstraction, based on the new quantum theories. During the age of the invention of the transistor [Arn98], around 1947, the results of an experiment [Mey47] could be explained using the Surface State Theory developed until that period of time,

but some time later, two experiments([Bra47] and [Sho48]) would be carried out confirming the existence of states at the surface.

W. Shockley, W. Read and R. Hall contributed to the field of surface states by presenting a mechanism that describes how charge carriers are trapped and recombined through sub-band gap states.

The basic mechanism whereby an electron is trapped by these sub-band gap states is shown by the following [Sho52]:

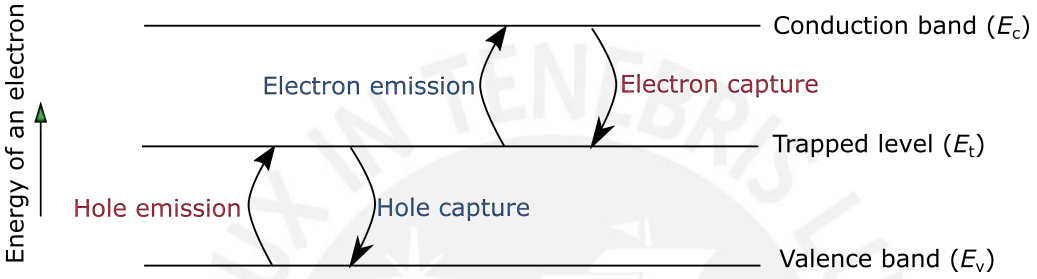

Figure 1.4: Shockley-Read-Hall recombination mechanisms

The investigation of the energy distribution of surface states in semiconductors allows to extend the Shockley-Read-Hall (SRH) Recombination Theory for an approximated energy-dependent continuum distribution which is represented by a density of surface states or interface trap density (D_{it}) that allows to define the net generation-recombination rate of charges at the surface as follows [Gou07]:

$$U_s = \int_{E_v}^{E_c} D_{it}(\epsilon_t) \cdot \frac{p_s \cdot n_s - n_i^2}{c_p^{-1}\left(n_s + n_1(\epsilon_t)\right) + c_n^{-1}\left(p_s + p_1(\epsilon_t)\right)} d\epsilon_t \tag{1.1}$$

where n_i is the intrinsic carrier concentration, p_s and n_s are the surface charge carrier concentrations for holes and electrons, respectively. p_1 and n_1 are the charge carrier concentration which depend on the energy difference between the trap state and the conduction band (for holes) and conduction band (for electrons). The values $c_{n,p}$ are the capture coefficients for electrons and holes, which are related to the effectiveness of the state to trap charges [Bla16; Bon17].

The generation rate of charge carriers depends on the temperature when the system is not under illumination, this rate is associated to the squared value of the intrinsic charge concentration whereas the product of surface charge carrier concentrations is associated to the recombination rate. Then the numerator, called the ”driving force” for recombination-generation processes [Fit68] could give information about

which kind of mechanism is dominating.

It is worth remembering that p_1 and n_1 depend on how deep is the state with respect to the bands edges. If these concentrations increase, i.e. if the state is closer to any of the bands edges, then the net recombination rate module decreases.

From the SRH recombination theory, it could be inferred, for electrons, that the emission processes for these shallower states compete with the capture mechanism, making the recombination mechanism less effective or less probable. Therefore, deep level states have a major contribution to the capture mechanism, which enhances its recombination probability.

L. Black [Bla16], using limiting cases, showed the range over which interface state recombination is greater than 90 % of the midgap value. In the case when the system is not under illumination could be around 0.7 eV. This range also depends on doping concentrations and fixed charges associated to a MOS system, therefore this is only a reference value. Taking as a reference the midgap D_{it} value, from -0.35 to 0.35 eV, out of this range recombination processes are significantly reduced by re-emission to bands mechanism.

Hence, recombination processes are strongly related to deep levels close to the midgap and motivate different topics related to interface or surface defect states.

From this theory, different parameters such as effective surface recombination velocity, surface saturation current density, among others, in order to evaluate a semiconductor surface were defined, and they are known as *surface recombination parameters* [McI14].

1.3 Surface Passivation

Surface passivation means to avoid or reduce charge carrier recombination via surface defect states by using a passivating layer on the silicon surface. This layer has the function to reduce the density of dangling bonds and, thus, available defects by means of stable bondings for these states. Furthermore, through a fixed charge density inside its volume, it repeals a type of concentration of charges at the surface in order to increase the re-emission mechanism of the trapped charges. The first one is known as Chemical passivation and the second one as Field effect passivation [Abe00] or Charge assisted passivation [Bon17].

These passivation mechanisms are characterized by two important parameters, one of them is the interface trap density $D_{it}(\epsilon_t)$, defined in section 1.2, which is highly related to the surface dangling bonds. The other mechanism is the Fixed charge density (slow states) Q_{fixed} or Q_{ox}, parallelly studied during the semiconductor revolution age by B. E. Deal who coined that term [Sch09].

These two parameters represent, quantify and show how the passivation properties of a semiconductor surface are. Many materials with different capabilities of applications were developed, as shown in figure 1.5.

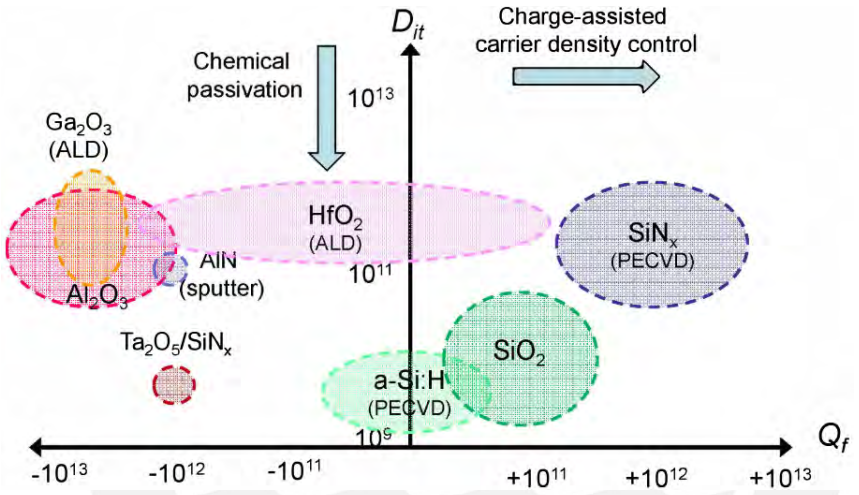

Figure 1.5: State of the art of passivating dielectric materials in function of the fixed oxide charges Q_f and the interface trap density D_{it} from ref. [Cue15].

Since Surface passivation depends on D_{it} and Q_{ox}, depending on the doping concentration, n-type or p-type, positive or negative fixed oxide charges is needed in order to reduce the recombination rate. The more optimizing passivation parameters are, the more efficient is the material to passivate the surface. Lower interface trap density and higher fixed oxide charges in absolute value are related to optimal conditions for chemical and charge assisted passivation respectively as shown in figure 1.5.

From the widely studied capacitance-voltage (with its wide range of types: High frequency, Quasi-static, thermal, etc.), conductance-voltage (G-V), Surface photovoltage, Deep Level Transient Spectroscopy (DLTS), among others [Nic82; Dit10] is possible to obtain information about them.

By obtaining passivation parameters, it is possible to explore into surface recombination parameters in order to have a better understanding about a certain device. For instance, solar cells could be characterized by different surface parameters according to models [Hau13]. Through parameters like surface recombination velocity,

dark saturation current and lifetime is possible to construct a realistic model [Gir88] for a device and simulate under different parameters and its capabilities [Hau13].

Science is a support for the technology, which represents at present part of consciousness.

1.4 Outline

The present work has the following outline: Chapter 2 shows a conceptual review about MOS systems, as well as the fundamental concepts related to HF-CV measurements. In this chapter the experimental procedure with the subsequent passivation parameter extraction will be summarized. After that, Chapter 3 will discuss the principal aspects related to the development of the HF-CV passivation parameters simulation tool. The aspects discussed here comprise equations, algorithms, features and some first results from simulated HF-CV curves based on simulated passivation parameters. A principal characteristic of the MOS system behaviour, the band-bending curve, is compared with results obtained using the *Multi-Dielectric Band-Diagram* program [Sou06] allowing to simulate the band diagrams related to a specific MOS system. Chapter 4 is dedicated to the validation and comparison of the simulation results of the developed tool with experimental data. In this sense, experimental passivation data of a thermal SiO_2 on crystalline silicon is evaluated. The experimentally extracted passivation parameters Q_{ox} and D_{it} are used in order to simulate HF-CV curves and then those curves are compared with the experimental one. A correction model algorithm is added based on the ideal curve, extracted from the experimental data, which was initially validated. Three types of D_{it} models is used in order to compare the simulated and measured HF-CV curves. By using an U-shape model for the D_{it} and from the developed simulator, an algorithm is proposed as an alternative approach, in order to approximate the D_{it} to the experimentally extracted. The algorithm is based on the combinatorial product rule of parameter values within approximated ranges whose result is derived from an approximation of the minimum mean square error. Finally the conclusions and outlook for this work are presented.

Chapter 2

High-Frequency Capacitance-Voltage characterization

Wir machen uns innere Scheinbilder oder Symbole der äußeren Gegenstände, und zwar machen wir sie von solcher Art, daß die denknotwendigen Folgen der Bilder stets wieder die Bilder seien von den naturnotwendigen Folgen der abgebildeten Gegenstände.

— Heinrich Hertz
DIE PRINZIPIEN DER MECHANIK IN NEUEM ZUSAMMENHÄNGE DARGESTELLT
(*Edited by Philipp Lenard*)

2.1 Representative images

In a certain region of space with a charge distribution, the total charge is proportional to the electric field through a Gaussian surface that confines this charge distribution. From the old Faraday's concept, the charge is proportional to the *number of lines of the electric field* [Fuc65]. If the total amount of charge increases in a certain quantity, the electric field (the number of lines) will increase proportionally. This is the Superposition Principle of Electric Fields [Fey63] as shown in figure 2.1.

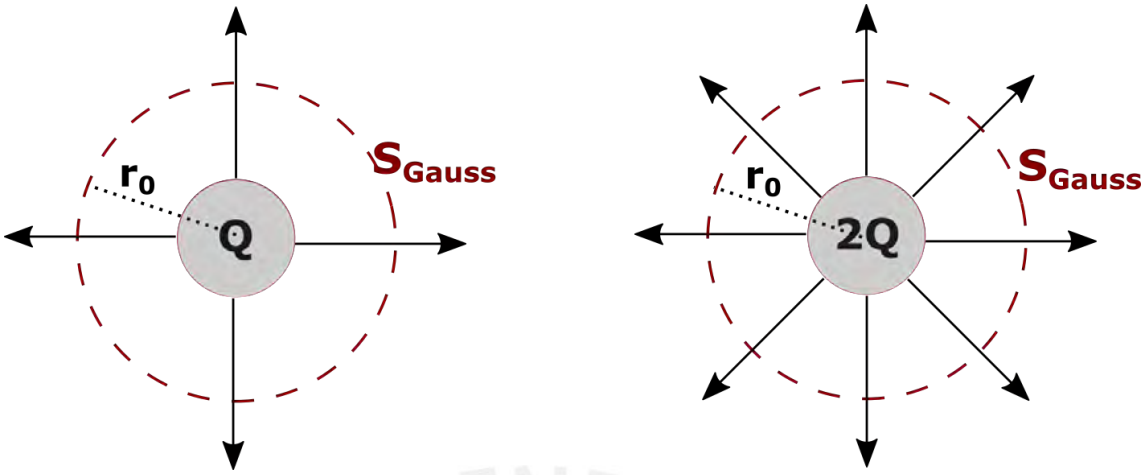

Figure 2.1: At the same distance to the center (in the Gaussian surface), the electric field in the right figure is exactly the double in comparison with the left figure

Due to this principle and since the total energy parameters are the potential difference and the total charge ($U = q\Delta V$), it is worth to define the capacitance as the ratio between the total charge in the system and the total potential difference or voltage. Thus,

$$C := \frac{Q}{\Delta V} \tag{2.1}$$

For evaluating the capacitance in a large range point to point (generally when the distribution of charge is not homogeneously distributed), the differential capacitance is defined as

$$C_{dif} := \frac{dQ}{dV} \tag{2.2}$$

According to this definition, it can approximate C_{dif} to a finite difference δQ per a finite change in the voltage δV. Using this approximation, it is possible to superpose a small time-dependent signal, with a given frequency for each voltage step obtaining in good approximation a linear response. This is the principle of the Small-Signal model. Therefore measurement of the capacitance in this manner will depend on the frequency.

In the following part, it will be referred to as differential capacitance simply as capacitance $C_{dif} = C$.

For a particular material, it is noticed that the way how this proportionality is given, between charge and voltage, depending on how these charges behave inside the material in the presence of an electric field. Metal, insulators, and semiconductors are some examples of materials and for the purpose exposed here, it is important to

consider them [Tar73].

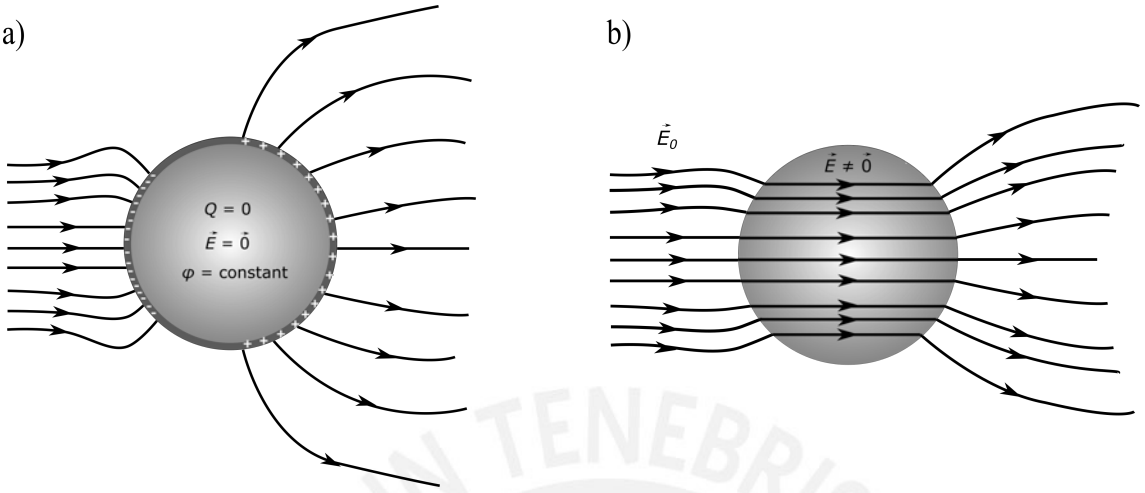

Figure 2.2: a) A neutral metallic conductor lie under an electrostatic field. The charge is polarized and distributed at the surface. b) If it is put a neutral insulator inside an electric field, this one is polarized volumetrically producing its own electric field (due to the total polarized charge) and the electric field through the insulator is the superposition of the surrounding electric field and the induced electric field.

A neutral metallic conductor, in presence of an electrostatic field, maintains its interior at the same potential, which means the electric field in the inside is null, whereas the polarized charges are distributed at the surface [Whi55; Pur85]. Actually the charges are distributed in a very thin layer, around 1 Å of thickness (figure 2.2a)) [Nic82]. Unlike metal, the charge belonging to a neutral insulator is totally polarized in the volume, as a result, a built-in electric field is originated doing the inner effective electric field less than the external electric field but different to zero as observed in figure 2.2b) [Pur85].

In order to have an idea about how charges behave inside a semiconductor in presence of an electrostatic field, the MOS (Metal-oxide semiconductor) capacitor is used which is made up by the junction (the physical model is based on the metallurgical junction) of a gate-metal, an oxide or in general an insulator and a semiconductor. The typical MOS is constructed based on Aluminium (gate-contact), thermally grown SiO_2 (oxide) and doped crystalline silicon(semiconductor) as shown in figure 2.3. In this particular example, it will be used a p-type crystalline silicon which has a convenient conductivity and will serve for this exposition. In order to have an energy reference, usually, an ohmic contact is deposited at the rear side of the MOS structure (which allow to have the exact same potential between the rear contact and the silicon bulk all the time).

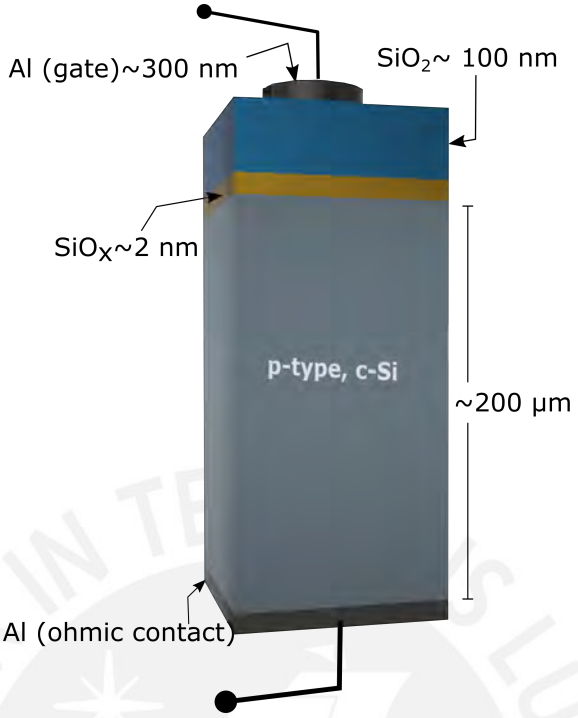

Figure 2.3: MOS capacitor structure based on crystalline silicon. Additionally the native layer of SiO_x is considered in this structure.

It will be used the same analogy applying forward to the entire system under an electric field. It can be made applying a voltage on the gate-contact. Intermediately, after the equilibrium is reached, polarization of charges at the oxide (whether induces by a gate voltage, fixed close to the interface, mobile in the bulk or trapped at the interface) induces a net charge inside the semiconductor, because of charge neutrality must be fulfilled this charges compensate the effect generated by the counter charges from the metal-oxide system. The region where these charges are spatially distributed is known as Space charge region, and it is susceptible, depending on the condition of the interacting system (metal-oxide), to compensate by different types of charges. On this fact lies the behaviour of charges in a semiconductor in presence of an electrostatic field. It could be interpreted that depending on the nature of the electric field, from positive or negatives charges (related to the orientation), and its intensity (related to the module) there are different responses of the semiconductor. The implied charges in the semiconductor are from three types: majorities, minorities charges, and ionized dopant (all charges, positive or negative, depends on the doping concentration). The presence of each type of charge defines three states: Accumulation (dominated by majority charge carries), inversion (dominated by minority charge carriers), and depletion (dominated, in general, by

ionized dopant). The pseudo-images (*Scheinbilder*) of the phenomenological nature of these charges lie in the quantum interpretation of the statistical mechanics applied to understand the electrical nature of the matter, but a deep explanation is out of the scope of this work.

With suitable assumptions [Kit57] the following energy diagram for the MOS system is constructed (see figure 2.4), assuming the common mechanism of charge transference for the ohmic contact: thermionic emission.

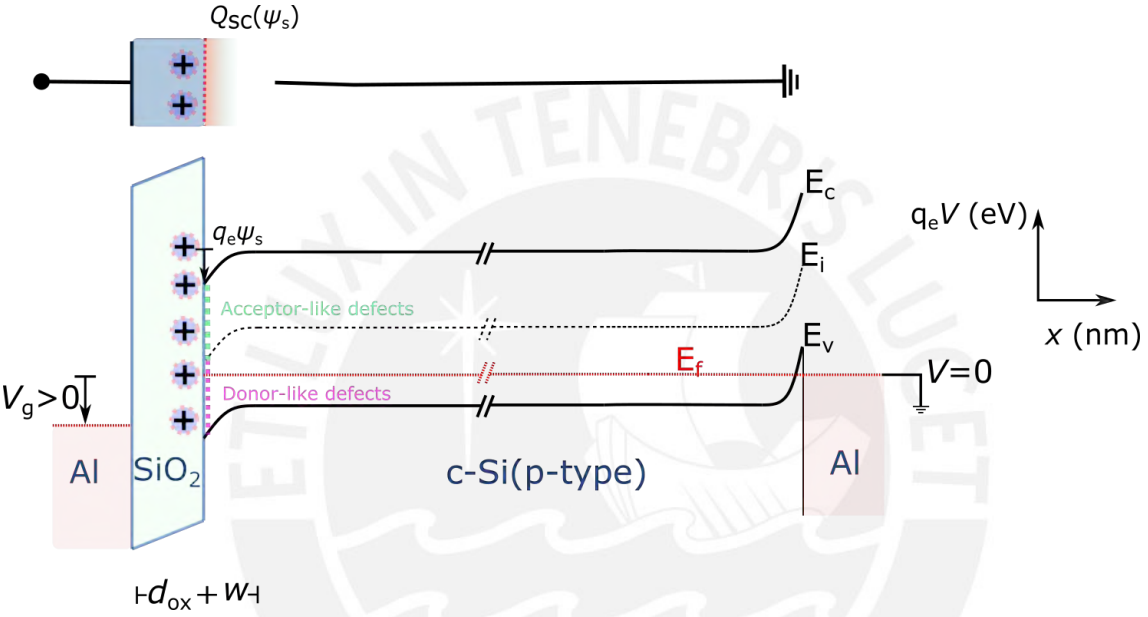

Figure 2.4: A net space-charge per unit area $Q_{sc}(\psi_s)$ is formed close to the interface, where the interfacial defects trap charges, whether acceptor- like or donor-like defects depending on the energetic level. Besides, rear ohmic-contact allows the assumption that bulk is practically at the same potential as the back-contact.

It is possible to use the concept about capacitance in this description, because similarly to the capacitor, this system stores electrical energy due to the implied charges when a voltage is applied. Thus mathematically this system is equivalent to a capacitance system [Nic82].

Doing an analogy with a parallel plate capacitor, parallel plates approximation states that the electric field is constant and homogeneous between the plates. As seen in figure 2.5, under the assumption that $b >> a$.

This means the effective zone where the capacitor concept holds true is just a little region, not the whole silicon bulk participate in the capacitor model. Since *Electric field lines go from the positive charges to negative charges*, therefore the capacitor is located just before the quasi-neutral region in the volume. If it is calculated

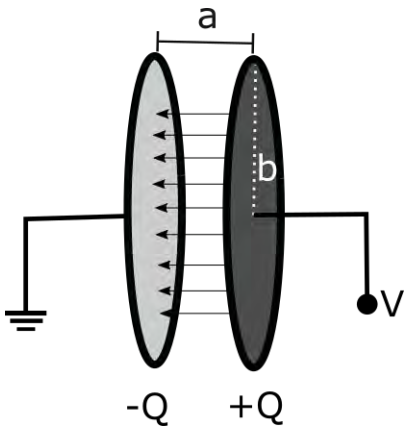

Figure 2.5: Parallel plates approximation means that the Electric field is enclosed and uniform between the plates

for a typical gate contact diameter (0.5 mm), the insulator thickness of 100 nm and assuming a space charge region length around 0.5 µm, $2b/a \approx 8.3 \times 10^2 >> 1$. This estimation considers the whole electric field constant, but for a semiconductor, due to the net charge is spatially distributed, the electric field is distance-dependent and confined within the capacitor region.

Then the quasi-neutral region is an equipotential region and generally is taken as the ground in the equivalent circuit. The total energy also is defined inside the capacitor, hence outside, the electrical energy must be zero with a good approximation. This means any additional elements (capacitances, inductances, resistances in the equivalent circuit) should not do decrease substantively the total energy. Furthermore, the total energy is distributed in the *equivalent circuit* with additional considerations like defects at the insulator-semiconductor interface and densities of charge inside the insulator. The ohmic contact with low specific resistance allows free movement of charge until the instantaneous equilibrium is reached.

Thermal equilibrium is an important concept for the considered model. That means the total charge behaves like a instantaneous completely charged capacitor from this it is possible to construct band diagrams for MOS devices as shown.

Certainly, if the Small-Signal treatment in order to measure the capacitance is applied, this would move the system from the equilibrium. It is worth to notice that the small signal ($V_{rms} \approx 15$ mV) ensures that the system behaves as a steady-state which means that despite a dissipation of energy is present, the representative characteristics of the system remain independent of the time.

The linear response ensures that it is possible to distinguish between the independent-

time and the dependent-time parameters when the mathematical description is made. It is assumed that all arguments is valid only for each voltage step. When a sweep is made, it is important to notice that the system has to be carried by steady state changes of the gate voltage, which means, the transition between two different steps is neglected.

With this consideration the sweep rate is defined, typically if the sweep rate is sufficiently slow so that generation and recombination of charges (majority and minority charge carriers) is allowed, then it is possible to obtain a characteristic Capacitance-voltage for the MOS system (CV curve). Depending on the positive or negative part of the superposed small signal, a generation or recombination of charges will be needed in order to fluctuate the charges with the signal frequency. Minority charge carriers has slow recombination-generation (R-G) rate than majority charge carriers due to those are generated in minor quantity by virtue of the absolute temperature T (in K).

For a frequency high enough (some hertz) minority charge carriers are not able to follow the small signal when the sweep rate is sufficiently slow. Then it is obtained a saturation in the part of the curve which is dominated for minority charge carriers. A typical frequency that allows to ensure the constant value of density of minority charge carriers without changes is the typical one standardized and widely studied 1 MHz [Nic82; Pie96; Sze07]. Then the High-Frequency Capacitance-Voltage (HF-CV) is the defined as the capacitance measured in these conditions.

Under these concepts and assumptions related to the HF-CV measurements, in this work, it is tried to elucidate ideas about the field aforementioned.

2.2 High-Frequency Capacitance-Voltage Method

In previous sections, conceptual ideas for the MOS capacitor were described. In this section, a description of the HF-CV measurements and the extraction process of MOS parameters is given.

2.2.1 Description of measurement and parameter extraction procedure

The typical MOS capacitor is based on a silicon wafer substrate. The wafer is cut in order to have adequate dimensions, which allows to manipulate it in order to proceed with the experiment (typically a squared form whose side is around a few cm). Standard cleaning processes, such as The RCA procedure, is used to remove organic and metallic contaminants and the HF-dip is used to remove the native oxide at the silicon surface [Rei18], contributing to a better surface passivation, according to [Bla16]. Thermally grown SiO_2 on c-Si with a subsequent forming gas anneal treatment ensures better passivation properties of silicon [Xia14]. Then, aluminum contact dots are deposited on the sample (typical dot diameters are between 0.5 mm to 1 mm). Finally, in most cases, aluminum in the rear side is carefully deposited in order to produce an ohmic contact.

Measurement set-up proceeds as is depicted in figure 2.6.

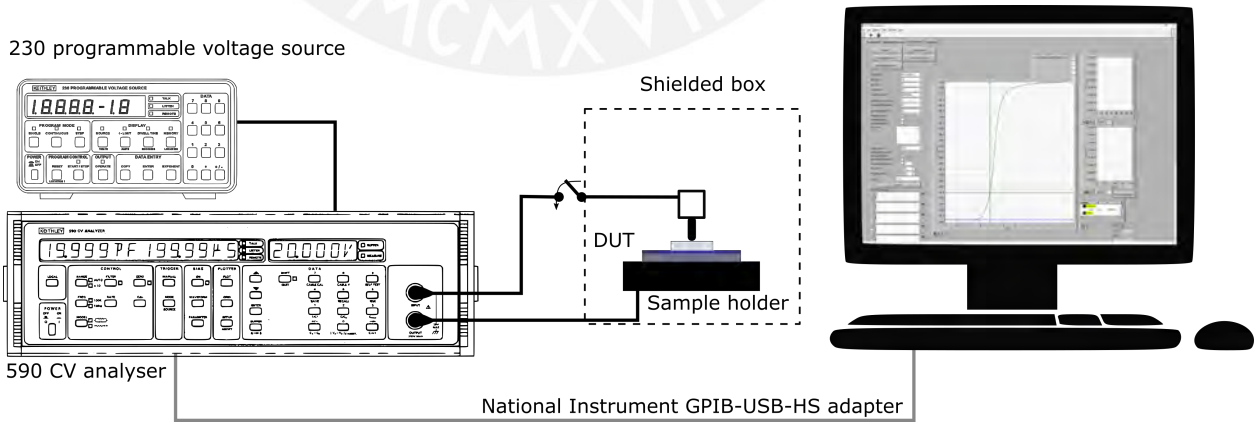

Figure 2.6: Here, the HF-CV measurement set-up is shown. The sample holder is provided by a measurement probe, this is placed on the contact dot carefully. The input signal is collected by this probe and the CV analyser output is connected to the other side by BNC cables. The PC communication is given by a GPIB-USB-HS adapter.

The device under test (DUT) is placed on the sample holder, ensuring good contact, using typically a membrane vacuum pump. Since the description about MOS capacitors was made for systems in steady-state conditions. The sample holder is located inside a metallic shielded box in order to isolate the system of light or another electromagnetic perturbation.

The measurements are performed through a HF-CV measurement set-up [Sta08]. This work is based on the Keithley 590CV analyser [KI99] measurements. Internally it has a sine wave synthesizer which on the one hand produces an AC signal, this signal pass through a transformer which converts it to a small signal of 15 mV rms. This AC small-signal is superposed to the bias voltage in order to use the afore-described model.

The involved measurement set-up count on an external Keithley 230 programmable source [KI92], this external source produces a voltage from $-100\,\mathrm{V}$ to $100\,\mathrm{V}$ whose range is suitable for a large variety of oxide thicknesses and different doping concentrations of silicon.

On the other hand, the signal synthesizer produces two orthogonal signals with phase shifts of 0° and 90°. The collected signal by the input probe is amplified as a first step. Since the input signal is buried to the noise, both orthogonal signals are used as a reference in order to use the quadrature phase-sensitive-detection which demodulates the signal proportional to the Capacitance. The capacitance signal is transmitted to the A/D converter, which converts the signal from analog to digital. These processes are controlled by an internal microprocessor (MPU) which communicates with a computer. In the diagram 2.7, typical communication is achieved by an IEEE-488 Bus. Here it is used a National Instrument GPIB-USB-HS adapter for this purpose.

To control this system, a measure-extraction program (the HF-CV Messprogramm) developed by Tim Henckel using LabView [Hen11] is manipulated. This program was made in base on the algorithms developed by Dr. Walter Füssel [Füs77], an interface specialist who widely explored into semiconductor interfacial phenomena and related techniques, mainly the Capacitance-Voltage technique.

Parameter extraction proceed as follow, the HF-CV system provides raw data about Capacitance-voltage (C-V), capacitance-time (C-t) and conductance-voltage(G-V) [KI99]. The first step is a smoothing of the curve through a fitting algorithm in order to remove the remaining statistical noise; then the smoothed $C(V_g)$ in pF and

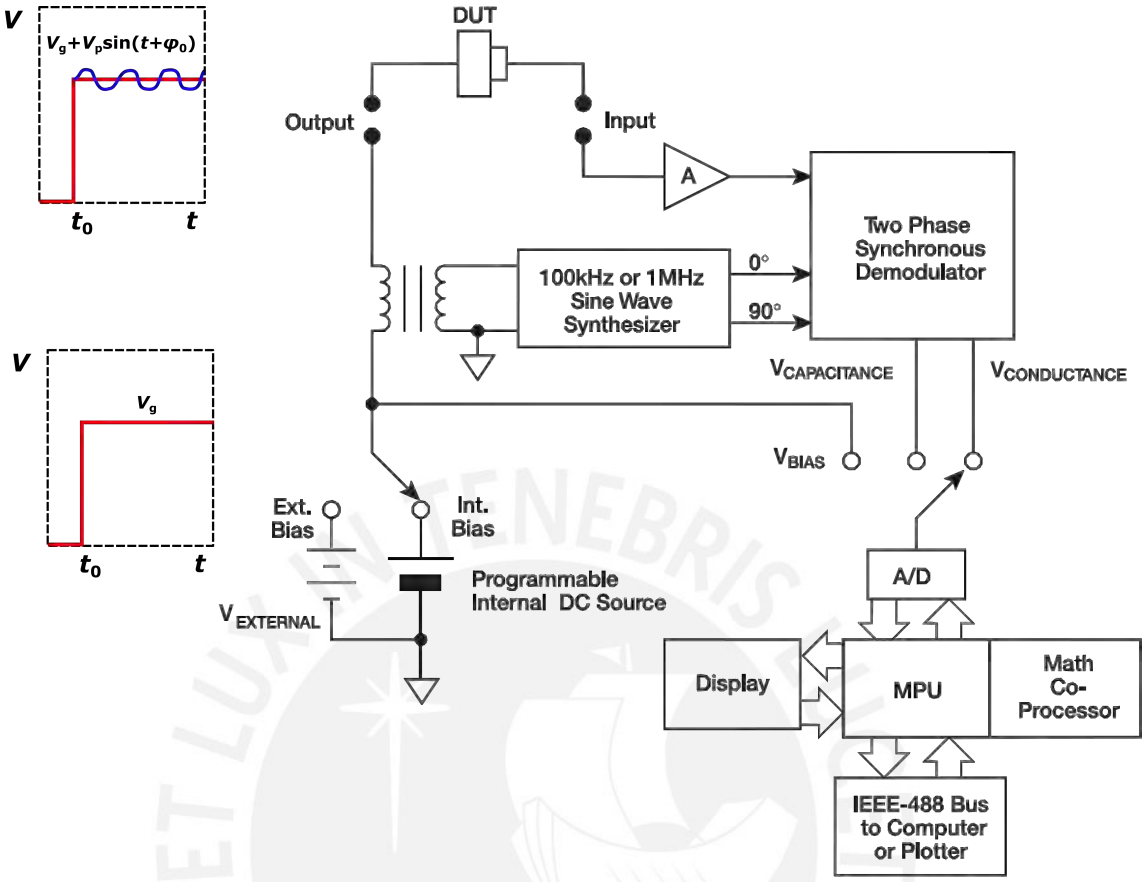

Figure 2.7: 590CV analyser [KI99]: The analyser allows to add an external bias which depends on the device to be measured, because the internal DC source have an scope from $-20\,\mathrm{V}$ to $20\,\mathrm{V}$. The device under test (DUT) is, in this work, a MOS capacitor and it is observed additionally how applied voltage in each step looks.

$dC(V_g)/dV_g$ in $\mathrm{pF\,V^{-1}}$ are obtained.

The contact area is very important for the following steps, since all subsequence subroutines depend on this parameter.

The contact area is inserted manually before to extract the normalized oxide capacitance C_{oxide} = (Oxide dielectric constant)/(Oxide thickness) (in $\mathrm{F\,cm^{-2}}$) and the doping factor λ = (Extrinsic doping concentration)/(Intrinsic doping concentration) (dimensionless) this two parameters define the theoretical HF-CV curve which is related to an ideal MOS system how it will be seen in section 3.2.

The iterative algorithm allows to find C_{oxide} and λ, both normalized by the contact area from the experimental capacitance curve. These two parameters (C_{oxide} and λ) depend on the oxide thickness and the doping concentration respectively which are possible to measure or to obtain an approximation. While extraction is being

performed, these parameters must be verified. Hence, the parameters extraction is a highly sensitive procedure which requires experimental criteria and knowledge of the model postulates.

Another iterative algorithm allows to extract the effect of the gate voltage (bias voltage) on the band-bending. This is related to the inner potential denominated surface potential ϕ_s in V. Thus, without any additional model the D_{it} is extracted from the experimental HF-CV curve, since the D_{it} depends on the HF-CV curve slope ($dC(V_g)/dV_g$) as follow [Füs77]:

$$D_{it}(q_e\phi_s) = \frac{C_{ox}}{q_e} \cdot \left[\left(\frac{C_{ox}}{C_{ox} + C_{sc}} \right)^2 \cdot \frac{dC_{sc}}{d\psi_s} \cdot \left(\frac{dC}{dV_g} \right)^{-1} - \left(1 + \frac{C_{sc}^{Lf}}{C_{ox}} \right) \right] \tag{2.3}$$

Where q_e is the elementary charge, C_{sc} is the capacitance formed in the semiconductor space charge region (which depend on the band-bending ψ_s) and C_{sc}^{Lf} is the capacitance of the space charge region at low frequency (Lf) which will be defined in the equation 3.16 in section 3.2. This last parameter depends on ψ_s and its expression is derived from the small-signal modelling.

This expression could be interpreted as follows,

Total capacitance is expressed (which is equivalent to expression 3.15 in section 3.2):

$$C = \frac{C_{ox} \cdot C_{sc}}{C_{ox} + C_{sc}} \tag{2.4}$$

If it is derived this expression in function of the ψ_s:

$$\frac{dC}{d\psi_s} = \left(\frac{C_{ox}}{C_{ox} + C_{sc}} \right)^2 \cdot \frac{dC_{sc}}{d\psi_s} \tag{2.5}$$

then, the expression 2.3 is reduced to,

$$D_{it}(q_e\phi_s) = \frac{C_{ox}}{q_e} \cdot \left[\frac{dC}{d\psi_s} \cdot \left(\frac{dC}{dV_g} \right)^{-1} - \left(1 + \frac{C_{sc}^{Lf}}{C_{ox}} \right) \right] \tag{2.6}$$

Since the interface trap density only makes sense for positive values under the MOS capacitor postulates, the right side factor also must be positive. Thus,

$$\left[\frac{dC}{d\psi_s}\cdot\left(\frac{dC}{dV_g}\right)^{-1}-\left(1+\frac{C_{sc}^{Lf}}{C_{ox}}\right)\right]>0 \tag{2.7}$$

Certainly, the sign of dC/dV_g is unknown because it depends on the doping type, then, a positive value is assumed.

Additionally, the C_{sc}^{Lf} definition (expression 3.16) is deduced in ref. [Füs77; Nic82] which simply relates the total derivative of the total space charge region charge in function to the band-bending, because responses of the charge carriers at low frequency are similar, which allows a simple deduction using the small-signal modelling.

In addition, the theoretical HF-CV curve depends on a specific voltage range, this voltage range is called the theoretical or the ideal voltage (V_{ideal} in V). The following expression is simply derived from these after-mentioned considerations:

$$\left|\frac{dV_{ideal}}{\psi_s}\right|=\left|1+\frac{C_{sc}^{Lf}}{C_{ox}}\right| \tag{2.8}$$

Since $dV_{ideal}/d\psi_s$ and $d\psi_s/dV_{ideal}$ can be defined implicitly (see expression 3.27). Thus, from equation 2.7:

$$\left|\frac{d\psi_s}{dV_{ideal}}\cdot\frac{dC}{d\psi_s}\right|>\left|\frac{dC}{dV_g}\right| \tag{2.9}$$

From the chain rule:

$$\left|\frac{dC}{dV_{ideal}}\right|>\left|\frac{dC}{dV_g}\right| \tag{2.10}$$

This last expression means that a positive D_{it} involves the slopes module of the experimental curve is smaller in comparison with the theoretical curve.

This algorithm is based on the Therman Method [Ter62] which implies a comparison of the ideal and the experimental HF-CV curves.

The effective oxide charge density is extracted from two characteristic points: midgap (MG) and Flatband (FB) conditions, the first one means the minority charge carriers and the majority charge carriers are compensated at the surface (bands bend until the Fermi level is located at midgap) and the second one means that any effects affect the bands and they remain flat.

Using a linear interpolation algorithm, two different effective oxide charge density are obtained but in this work, $Q_{ox,eff}$ at midgap is used, because, at this point, effects of the surface state are neglected (almost null).

Additionally, capacitance-time curves allow to evaluate the charge carriers responses reliability, since for each bias voltage a specific time related to R-G processes is needed in order to construct the HF-CV curve. This topic will be described with detail in section 4.3.

2.3 Conclusion

The capacitance is defined as a system property of storing charges for a given potential difference. This concept is extended to define a Metal-Oxide-Semiconductor (MOS) system. Since this property depends on the MOS geometry, the band diagram was introduced. The implied mechanisms were explained conceptually based on the charge carriers (electrons and holes) and the ionized dopants. These concepts were used to explain the HF-CV measurement, which is the principal topic of this work.

Once the general concepts about the MOS capacitor were discussed, in the subsequent section, the measurement process and extraction of passivation parameters through the HF-CV Messprogramm will be exposed. The HF-CV technique involves the capacitance measurement through the quadrature sensitive detection which extracts capacitance signal from the buried in a noise environment.

The extraction algorithm was described taking into account sensitive parameters as the contact area which is manually inserted. The D_{it} extraction is based on the equation which takes into account the slopes of the ideal and experimental curves. The effective oxide charge density which is extracted at midgap, and the extracted D_{it} represent the passivation parameters.

Chapter 3

Development of HF-CV curves simulations based on simulated passivation parameters

I didn't think; I investigated
— Wilhelm Röntgen

3.1 Introduction

In this chapter, some aspects of the model and the algorithms along with the general program characteristics are described.

The program was developed using Python 3.6 because it is principally an open-source software, which allows to share tools between the scientific community.It is easy to use and it has packages that allow to manipulate scientific data. Therefore, its popularity has been growing in the last years [SO19].

The MOS system model description is based on the results of solving the unidimensional classical Poisson equation assuming a concentration of charges under the Boltzmann approximation ($T \sim 300\,\mathrm{K}$) [Sho63]. The classical treatment is sufficient for the passivation phenomena of the sample studied in this work.

The Poisson Equation solution allows to obtain the band-bending dependent of

Physical constants		
Constant	Description	Value
q_e	Elementary charge (C)	$1.602176462 \times 10^{-19}$
K_B	Boltzmann constant($\mathrm{J\,K^{-1}}$)	$1.3806503 \times 10^{-23}$
ϵ_0	Vacuum permittivity ($\mathrm{F\,cm^{-1}}$)	$8.85418781762 \times 10^{-14}$
ϵ_{si}	Silicon relative permittivity ($*$)	11.8
ϵ_{ox}	Oxide relative permittivity ($*$)	3.8

Table 3.1: Physical constants used in the frame of this work.

the total space-charge per unit area, $Q_{sc}(\psi_s)$. Using this quantity and taking into account the $\psi_s - V_g$ dependence, the HF-CV curve can be constructed. The ideal HF-CV curve considers the effect of the metal-semiconductor work-function difference.

The HF-CV curve is derived from an exact solution and a closed-form approximation developed by Lindner [Lin62] with an enhancement made by Fenske [Fen83].

Because of the interest in expanding its applicability scope, this tool has public access in GitHub (Migusb). In the next chapter, the simulation reliability will be tested comparing simulations with experimental data.

3.2 Model and algorithm description

In order to construct the HF-CV curve, the capacitance as a voltage function is measured for each gate-voltage according to section 2.1. Assuming mainly the Band-Bending approximation [Nic82], the electric field through the semiconductor is solely in charge of energy changes of conduction and valence band edges. Then, a relationship between the voltage and changes of band edges is needed. The concentration of charges will depend on these energy changes. Some potentials associated with the semiconductor due to these energy changes are defined as depicted in Figure 3.1.

The physical constants used in this work are summarized in table 3.1.

The surface potential is defined as the difference between the Fermi level (E_f) and the intrinsic Fermi level at the surface ($E_i^{surface}$) both in eV:

$$q_e \phi_s = E_f - E_i^{surface} \tag{3.1}$$

The bulk-potential (in V), which is independent on the gate voltage, is defined using

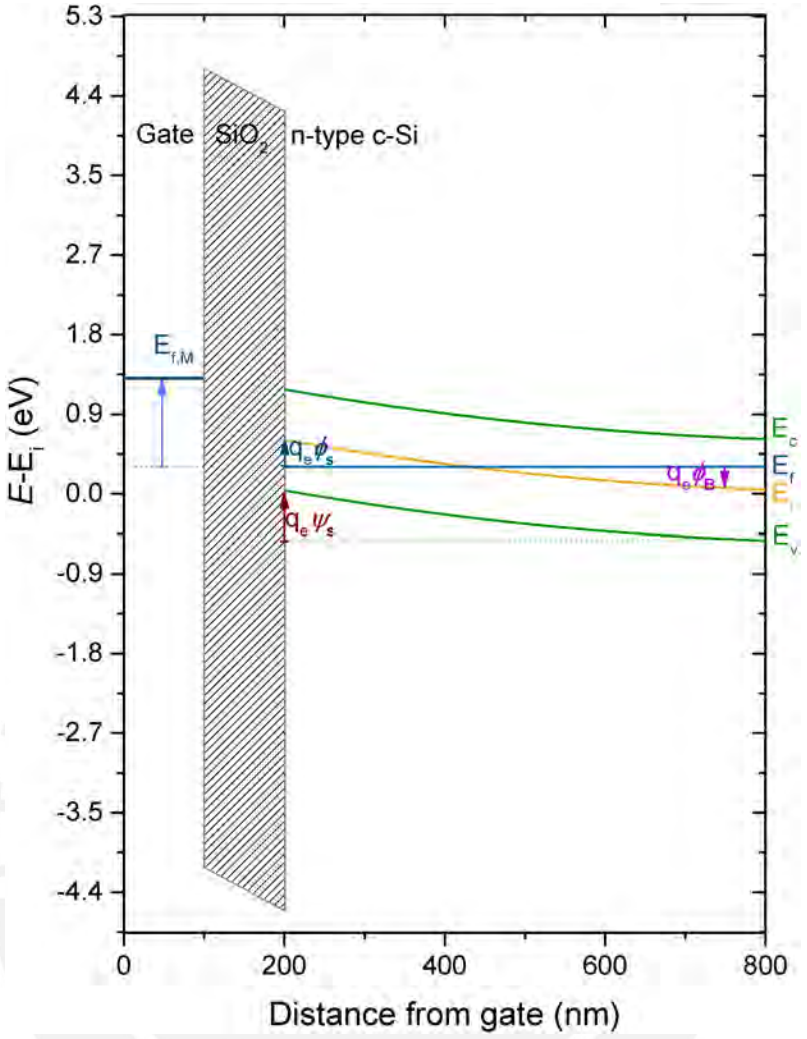

Figure 3.1: Simulated band-diagram of a Al/SiO_2/c-Si system through the *Multi-Dielectric Band-Diagram* program [Sou06] showing the associated potentials.

the intrinsic Fermi level inside the bulk, in the quasi-neutral region:

$$q_e\phi_B = E_f - E_i^{quasi-neutral} \tag{3.2}$$

Since the Fermi level depends on the net doping concentration, donors for n-type c-Si (N_D) or acceptors for p-type c-Si (N_A) in cm^{-2}, the bulk-potential is defined for each type.

For n-type c-Si:

$$\phi_B^{donors} = \frac{K_B T}{q_e} \cdot ln\left(\frac{N_D}{n_i}\right) \tag{3.3}$$

and for p-type c-Si:

$$\phi_B^{acceptors} = -\frac{K_B T}{q_e} \cdot ln\left(\frac{N_A}{n_i}\right) \tag{3.4}$$

n_i depends mainly on the temperature T. The following expression is used [Pie95] which is the same expression used to the HF-CV Messprogramm [Hen11]:

$$n_i(T) = 9.15 \times 10^{19} \left(\frac{T}{300}\right)^2 e^{\frac{-6880}{T}} \tag{3.5}$$

Additionally, the band-bending (in V) is defined as:

$$\psi_s = \phi_s - \phi_B \tag{3.6}$$

The corresponding normalized potentials (dimensionless) is defined as follows:

$$v_s = \frac{q_e \psi_s}{K_B T} \tag{3.7}$$

$$u_s = \frac{q_e \phi_s}{K_B T} \tag{3.8}$$

$$u_B = \frac{q_e \phi_B}{K_B T} \tag{3.9}$$

Once the charge carrier concentration was defined from these potentials, the density of charges and potentials at the system are associated by the Poisson Equation. The Poisson Equation can be solved with quantum mechanical treatments or by classical approximations. In this work, the classical model was used. Solving the Poisson Equation, the semiconductor *dimensionless* electric field (dependence on v_B is assumed) is determined by:

$$F(v_s) = (2)^{1/2} \left[(-v_s)\, sinh\,(u_B) - (cosh\,(u_B) - cosh\,(v_s + u_B))\right]^{1/2} \tag{3.10}$$

and the charge carrier density that depends on ψ_s or v_s (in $\mathrm{C\,cm^{-2}}$) is:

$$Q_{sc}(v_s) = Sgn(-v_s) \cdot \frac{\epsilon_0 \epsilon_{si}}{\lambda_i} \cdot \frac{K_B T}{q_e} \cdot F(v_s) \tag{3.11}$$

Where λ_i and $\lambda_{n,p}$ (in cm) are the intrinsic and extrinsic (n- and p- type c-Si) Debye length respectively:

$$\lambda_i = \left(\frac{\epsilon_s K_B T}{2 q_e^2 n_i}\right)^{1/2} \tag{3.12}$$

$$\lambda_{n,p} = \left(\frac{\epsilon_s K_B T}{q_e^2 N_{D,A}} \right)^{1/2} \tag{3.13}$$

Based on the Small-Signal modelling, an equivalent circuit of the MOS device is associated. Two capacitances in series are designed: one of them, the oxide capacitance here is redefined (defined in section 2.2.1) as C_{ox} in F. By a few changes in the algorithm, it is possible to obtain the total capacitance in F, but as it will be shown. The normalized oxide capacitance is obtained by,

$$C_{ox} = \frac{\epsilon_0 \cdot \epsilon_{ox} \cdot S}{d_{ox}} \tag{3.14}$$

Where S (in cm^{-2}) is the gate contact area and d_{ox} (in nm) is the oxide thickness.

Therefore, through the space-charge region capacitance per unit area C_{sc} (in $\mathrm{F\,cm}^{-2}$), the total capacitance C_{total} is expressed as:

$$\frac{1}{C_{total}} = \frac{1}{C_{sc}\left(\psi_s\right)} + \frac{S}{C_{ox}} \tag{3.15}$$

The HF-CV characteristic shape is constructed based on this relationship. As mentioned, the majority and minority charge carries have different R-G rates, hence their responses to the frequency will be according to that rates.

At Low-Frequency, the majority and minority charge carriers responses to the small changes in the voltage are due to the superposed small-signal. The MOS model suggests to calculate the Low-Frequency differential capacitance per unit area at the space-charge region C_{sc}^{Lf} as:

$$C_{sc}^{Lf} = \left(-\frac{dQ_{sc}}{d\psi_s} \right) \tag{3.16}$$

Solving 3.16 with 3.11:

$$C_{sc}^{Lf} = Sgn(v_s) \cdot \left(\frac{\epsilon_s}{\lambda_i} \right) \cdot \frac{sinh(v_s + u_B) - sinh(u_B)}{F(v_s)} \tag{3.17}$$

By replacing this expression into the equation 3.15, C_{total}^{Lf} is found.

At High-Frequency, the minority charge carriers, due to its low R-G rate, are not

able to follow the AC-signal. Thus, the minority charge carriers need more time than the majority charge carriers in order to reach the steady-state response of the gate-voltage. This time depends on the sweep rate which was commented in section 2.1.

In order to derive an expression for the semiconductor capacitance, the minority charge carriers response must be considered. The inversion bias condition is constructed by the minority charge carries. Since the small AC-signal makes not change the total amount of the minority charge carries, this quantity must remain fixed and will give rise to a saturation condition. Another effect related to the spatial movement of charge at the semiconductor interface is taken into account. Therefore, the minority charge carrier density or also called the inversion layer is almost fixed and the inversion layer thickness fluctuates from the wider to narrower thickness and vice versa depending on each cycle of the AC small signal. With this considerations, the High-frequency differential capacitance per unit area at space-charge region C_{sc}^{Hf} is constructed for p-type silicon [Bre74; Pie95]:

$$C_{sc}^{Hf,exact} = \frac{\lambda_i}{\epsilon_0 \epsilon_{si}} \left[\frac{2 \cdot F(v_s)}{e^{u_B}\left(1 - e^{-v_s}\right) + e^{-v_s}\left(e^{v_s} - 1\right)\left(\frac{1}{1+\Delta}\right)} \right] \tag{3.18}$$

Here, Δ is 0 for $v_s < \phi_B$, which makes $C_{sc}^{Hf,exact} = C_{sc}^{Lf}$ otherwise it has the following expression:

$$\Delta = \left(e^{v_s} - v_s - 1\right) \left[F(v_s) \int_{u_B}^{v_s} \frac{e^{u_B}\left(1 - e^{-v_s}\right)\left(e^{v_s} - v_s - 1\right)}{2F^3(v_s)} dv_s \right]^{-1} \tag{3.19}$$

u_B is taken as the lowest limit in the integral as suggested in ref. [Nic82] but also it could be taken from 0 because minority charge carriers at the space charge region for the range of $0 < v_s < u_B$ (Depletion) have a negligible influence on the capacitance.

Since voltages are symmetrical for p- and n-type MOS devices as suggested in ref. [Pie95], it is enough to replace V_g by $-V_g$ in the p-type equations in order to produce the curve for the n-type capacitor. This suggestion is used in the developed simulation tool. The algorithm described by R. Pierret in ref. [Pie95] to solve the exact solution is taken into account.

A *closed-form approximation* solution was developed by Lindner in Ref. [Lin62], but the relative error increases in inversion. An enhancement to this approximation in

inversion is made by taking into account the *match point* which allows to have a saturation capacitance in inversion.

Thus, for p-type:

$$C_{sc}^{L} = 2^{-1/2} \cdot Sgn(v_s) \cdot C_{FBS} \left[1 - e^{-v_s}\right] \left[(v_s - 1) + e^{-v_s}\right]^{-1/2} \tag{3.20}$$

and for n-type:

$$C_{sc}^{L} = 2^{-1/2} \cdot Sgn(v_s) \cdot C_{FBS} \left[e^{v_s} - 1\right] \left[-(v_s + 1) + e^{v_s}\right]^{-1/2} \tag{3.21}$$

Where C_{FBS} is denominated the silicon *flatband* capacitance:

$$C_{FBS} = \frac{\epsilon_0 \cdot \epsilon_{si}}{\lambda_{n,p}} \tag{3.22}$$

The match-point v_m is used as follows,

$$C_{sc}^{Hf}(v_s) = C_{sc}^{L}(v_s); \qquad v_s < v_m \tag{3.23}$$

and

$$C_{sc}^{Hf}(v_s) = C_{sc}^{L}(v_m); \qquad v_s > v_m \tag{3.24}$$

The Lindner match-point is derived from:

$$e^{v_m^L} = v_m^L - 1 \tag{3.25}$$

A simple improvement of this approximation was made by F. Fenske [Fen83] which modifies the expression as:

$$v_m = v_m^L - 2.25 \tag{3.26}$$

which is used in the developed simulation tool.

Since the capacitance depends explicitly on the band-bending, an expression that relates the band-bending with the gate-voltage is needed. According to the Small-Signal modelling, the following expression that takes into account the work-function difference factor per elementary charge W_{ms} (in V), is derived:

$$V_g = \psi_s(V_g) - \frac{Q_{sc}(\psi_s(V_g)) \cdot S}{C_{ox}} + W_{ms} + \phi_B \tag{3.27}$$

where W_{ms} has the following expression:

$$W_{ms} = \Phi_m - (\Phi_s - \phi_B) \tag{3.28}$$

To construct the simulation tool $\Phi_m - \Phi_s = -0.22\,\mathrm{V}$ is considered from ref. [Wer74] which corresponds to the difference in the work-function between aluminium and intrinsic silicon.

In equation 3.27 is clear that the band-bending depends on the gate-voltage, therefore the explicit dependence $\psi_s(V_g)$ is expressed as a cause-effect relationship.

The equation 3.27 constitutes an implicit equation. Since the range of the band-bending is known, it is enough to extract the gate-voltage from this equation, which means to produce V_g from a supposed ψ_s [Pie95]. But here, in order to verify simulations with experimental data, any gate-voltage can be applied, which means, ψ_s does not need to be previously known, hence the implicit equation must be solved.

An approach to obtain a numerical solution was performed using the bisection method [Pre07] because only two extreme points are needed to solve it, although the convergence is reached slowly in comparison to other methods [Pre07].

Once ψ_s is obtained from V_g, inserting the other parameters from the MOS system into the equations 3.21,3.20,3.18, 3.15, simulations of ideal HF-CV curves are obtained as depicted in figure 3.2.

Since W_{ms} has a constant component (the work-function difference for the aluminum and intrinsic silicon) this provides a shift of the curve. Besides, $W_{ms} < 0\,\mathrm{V}$ and according to equation 3.27 which involves a net shift to the left side of the HF-CV curve independent on the doping type.

The closed-form approximation shows significant deviation from the exact solution curve in inversion, while in depletion and accumulation is very approximated to the exact one.

The principal parameters (with a fixed absolute temperature T) for simulating the ideal HF-CV curve for the MOS system according to the MOS model described in this chapter are d_{ox} and N_d. They must be carefully extracted as described in section

2.2.1.

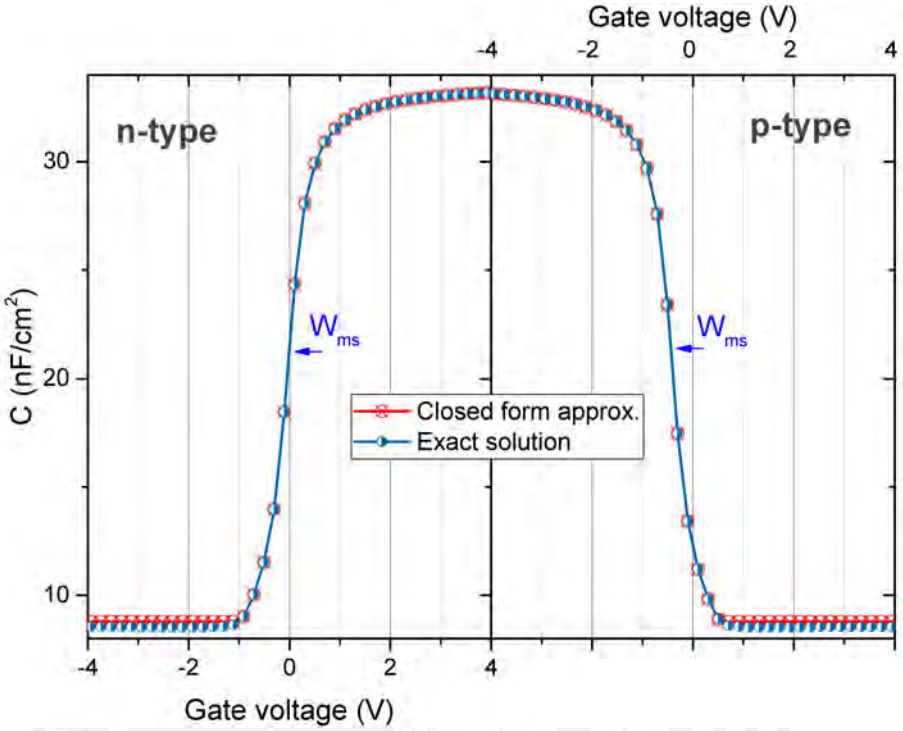

Figure 3.2: Simulation of the ideal ($Q_{ox} = 0$,$D_{it} = 0$) HF-CV curves for n- and p-type c-Si: $T = 300\,\mathrm{K}$, $d_{ox} = 100\,\mathrm{nm}$, $N_d = 1 \times 10^{15}\,\mathrm{cm}^{-2}$. Metal-semiconductor Work-function difference factor W_{ms} is included. Both curves present a small shift due to W_{ms}.

The following part of this work is focused on introducing simulated passivation parameters in order to investigate its effects on the HF-CV curve.

On the one hand, the first non-ideality to be considered is the effective oxide charge density $Q_{ox,eff}$. The oxide charges may be composed by mobile and fixed trapped charges (Q_f).

Mathematically, this effective oxide charge density is expressed by the following equation [War99; Sch09] with d_{ox} measured from the semiconductor-insulator interface and ρ_{ox} as the mobile charge density:

$$Q_{ox,eff} = \frac{1}{d_{ox}} \int_0^{d_{ox}} x \cdot (Q_f \delta(x - d_{ox}) + \rho_{ox}(x))\, dx \tag{3.29}$$

From the equation 3.29, and the fact that fixed charges are located very close to the semiconductor-insulator interface, $Q_{ox,eff}$ approximates to Q_f whereas the mobile

charges density, which is distributed in the whole insulator volume, can be neglected in most cases.

Therefore, $Q_{ox,eff}$ is related to the Charge assisted passivation (described in section 1.3).

On the other hand, the D_{it} is an energy-dependent function. In order to introduce it on the HF-CV curve simulation, it will be used three different models.

As depicted in figure 2.3 a very thin layer ($\sim$ 2 nm) of SiO_x is formed naturally when thermal SiO_2 is deposited con c-Si. This very thin layer plays an important role during silicon surface passivation [Nic82; Sze07].

The currently accepted D_{it} model in the scientific community is based on P_b defects at SiO_x/Si interface which also depends mainly on the silicon crystal orientation, on the surface, pre-deposition surface cleaning or wet-chemical treatments, deposition parameters and conditions. Different types of defect centers (P_b, P_{b0} and P_{b1}) can be distinguished of which P_{b0} and P_{b1} are exclusively formed for the (100) silicon crystal orientation. This work is focused on this particular silicon crystal orientation. In addition, the radicals $\cdot Si{\equiv}Si_3$ and $\cdot Si{\equiv}Si_2O$ at the c-Si interface are associated to the P_{b0} and P_{b1} defects respectively [Ent07] .

Due to the amphoteric nature of these defects, their energy distribution for each defect includes two different peaks in the silicon band gap. As a consequence, two Gaussian functions can be associated to the defect centers and found on each side of the silicon band gap (Lower: L, between E_v and the midgap and Higher: H, between the midgap and E_c).

Strained bond defects at this interface are represented by exponential functions $U_{T,v \text{ and } c}$ located near each band edge.

Thus, for a trap state with an energetic value of ϵ_t (in eV) within the silicon band gap, the following functions associated with each defect type are defined:

$$P_{b0}^{L,H}(\epsilon_t) = \frac{N_t^{Pb0L,H}}{w_{L,H}\sqrt{\frac{\pi}{2}}} e^{-2\frac{\left(E_{0L,H}-\epsilon_t\right)^2}{w_{L,H}^2}} \tag{3.30}$$

$$P_{b1}(\epsilon_t) = \frac{N_t^{Pb1}}{w_1\sqrt{\frac{\pi}{2}}} e^{-2\frac{(E_1-\epsilon_t)^2}{w_1^2}} \tag{3.31}$$

$$U_{T;v,c}(\epsilon_t) = N_{v,c} e^{-\beta_{v,c}|E_{v,c}-\epsilon_t|} \tag{3.32}$$

Where $N_t^{Pb0L,H}$ and N_t^{Pb1} are the amplitudes of the Gaussian distributions related to P_{b0} and P_{b1} respectively, $w_{L,H}$ and w_1 are the Gaussian distribution widths, $\beta_{v,c}$ are parameters related to the exponential functions slope, $E_{0L,H}$ E_1 are the center of the Gaussian distribution whereas $E_{v,c}$ are the energetic position of the exponential functions for the strained bonds.

Experimental facts about this model suggest to consider approximations for some parameters so that they restrict the value which these parameters could take. These restrictions can be reviewed in ref. [Ger86; Fli95] and are used also in ref. [Töf14]: $\beta_{v,c} \approx 40\,\mathrm{eV}^{-1}$, energetic separation between P_{b0}^L and P_{b0}^H is around 0.7 eV, while for P_{b0}^L and P_{b1} is around 0.29 eV. This facts are used in order to simulate the D_{it} based on the Gaussian Distribution Model[Fli95; Li19; Ger86; Rag99; Bro88; Hel94; Cam02; Len98].

Therefore, the D_{it} can be modelled by the total sum of the afore-mentioned defect types:

$$D_{it}(\epsilon_t) = N_v e^{-\beta_v|E_v-\epsilon_t|} + \frac{N_t^{Pb0L}}{w_L\sqrt{\frac{\pi}{2}}} e^{-2\frac{(E_{0L}-\epsilon_t)^2}{w_L^2}} + \frac{N_t^{Pb1}}{w_1\sqrt{\frac{\pi}{2}}} e^{-2\frac{(E_1-\epsilon_t)^2}{w_1^2}} + \frac{N_t^{Pb0H}}{w_H\sqrt{\frac{\pi}{2}}} e^{-2\frac{(E_{0H}-\epsilon_t)^2}{w_H^2}} + N_c e^{-\beta_c|E_c-\epsilon_t|} \tag{3.33}$$

Since the Gaussian Model has a significant number of parameters, a simple U-shape model using the exponential state tails of the Gaussian model is presented. In order to construct this U-shape model, a constant function along with the exponential functions are considered. The constant function, defined as D_{it}^0 defines the D_{it} at midgap and replaces the three Gaussian functions. Therefore, the nine parameters related to Gaussian distributions is reduced to only one parameter: D_{it}^0.

$$D_{it}(\epsilon_t) = N_v e^{-\beta_v|E_v-\epsilon_t|} + D_{it}^0 + N_c e^{-\beta_c|E_c-\epsilon_t|} \tag{3.34}$$

This model will be used in section 4.3 when experimental data will be analysed.

For the purpose of observing the effect of the interface trapped charges on the HF-

D_{it} simulation parameters			
Dangling bond	$N_t^{P_{b0L}}$, $N_t^{P_1}$, $N_t^{P_{b0H}}$ (cm^{-2})	w_L, w_1, w_H (eV)	E_{0L}, E_1, E_{0H} (eV)
P_{b0}^L	5.0×10^{10}	0.24	-0.375
P_{b1}	6.0×10^{10}	0.34	0.000
P_{b0}^H	5.0×10^{10}	0.16	0.325
Strained bond	N_v, N_c (cm^{-2})	β_v, β_c (eV^{-1})	E_v, E_c (eV)
$U_{T,v}$	2.0×10^{14}	40	-0.56
$U_{T,c}$	2.0×10^{14}	40	0.56

Table 3.2: Simulations parameters based on the Gaussian model.

CV curves, a D_{it} shaped using the Gaussian model is simulated as depicted in figure 3.3. The simulation parameters are summarized in the table 3.2 according to the Gaussian model.

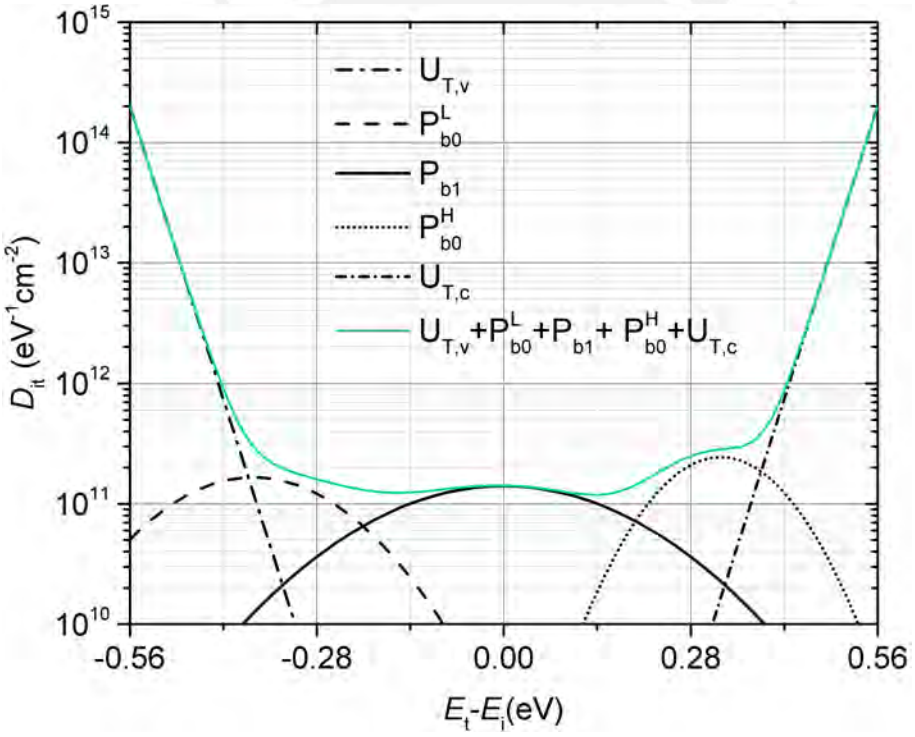

Figure 3.3: D_{it} simulated by a Gaussian model with each defect center contribution. The simulation parameters are summarized in table 3.2

The above mentioned amphoteric nature of defects behaves as follows, depending on where the Fermi level is, in reference to the E_0 level (suggested to be close to the midgap in ref. [Sze07]): On the one hand, the donor-like trap when is non-occupied, it is positive, whereas, if it is occupied it behaves neutrally, on the other hand, the acceptor-like trap is neutral when it is non-occupied and if it is occupied, it is negative .

The Fermi-Dirac statistic will be applied to the interface trapped charges, which depends on the surface potential which, in turn, depends on the gate voltage. In order to obtain the general expression, a shift of the Fermi function in ϕ_s units is taken into account. From the sign convention, the general expression of interface trapped charges $Q_{it}(\phi_s)$ (in $\mathrm{C\,cm^{-2}}$) could be constructed in a geometrical manner, as shown in figure 3.4. This expression takes into account the experimental ϕ_s sweep. It is senseless to consider the entire band gap range if, from the experiment, the bands bend just until a lower limit than the band edges.

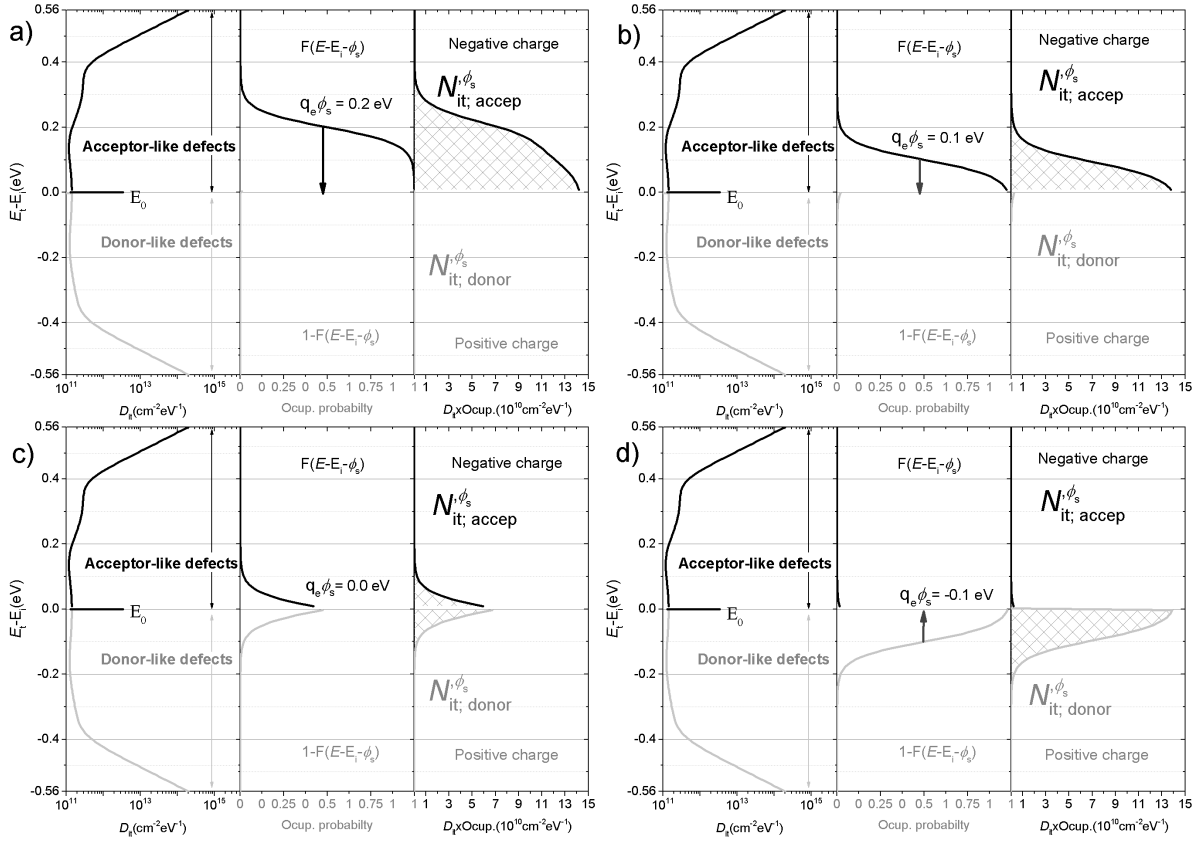

Figure 3.4: $Q_{it}/q_e = N_{it}$ ($N^{\phi_s}_{it,acc}$ acceptor- and $N^{\phi_s}_{it,donor}$ donor-like defects) simulated through the D_{it} Gaussian model using $g = 1$.

As seen in figure 3.4, the simulation only takes into account the D_{it} function and the Fermi distribution Function ($F(E-E_i-\phi_s)$) related to the probability of a charge to be trapped by a surface state, which means the same function can be used for n- and p-type silicon. Choosing n-type silicon as an example, ϕ_s dictates what bias condition is, thus: a) shows the accumulation condition for $q_e\phi_s = 0.2eV < q_e\phi_B = 0.29eV$, b) Depicts also accumulation but in this case $N^{\phi_s}_{it,acc}$ decreases because it depends on the $q_e\phi_s$ module. c) shows the midgap condition, when net Q_{it} is approximately null.

Additionally, $N_{it,acc}^{\phi_s} \approx N_{it,donor}^{\phi_s}$. d) shows inversion bias condition, ϕ_s is inverted and the positive contribution in the net Q_{it} increases. As observed, this analysis was made from ϕ_B, this quantity is an intrinsic potential of the semiconductor. For a p-type semiconductor $\phi_B < 0$ then, according to the comparison between ϕ_B and ϕ_s, the bias condition can be determined.

Thus:

$$Q_{it}(q_e\phi_s) = q_e \int_{q_e\phi_s^i}^{E_0} D_{it}^d(q_e\phi_s)\cdot[1-f_0(\epsilon_t-\epsilon_i-q_e\phi_s)]d\epsilon_t - q_e \int_{E_0}^{q_e\phi_s^f} D_{it}^a(q_e\phi_s)\cdot f_0(\epsilon_t-\epsilon_i-q_e\phi_s)d\epsilon_t \tag{3.35}$$

The Fermi function [Nic82; Sze07] is centered in 0 eV:

$$f_0(\epsilon_t) = \frac{1}{1+g\cdot e^{\frac{\epsilon_t}{K_B T}}} \tag{3.36}$$

Where g is the degeneracy factor which is related to the single occupation of defects [Nic82]. It will be considered $g = 1$ only for practical purposes. More accurate results can be obtained using $g = \frac{1}{2}$.

Considering the passivation parameters, the equation 3.27 is modified as follows:

$$V_g = \psi_s(V_g) - \frac{Q_{sc}(\psi_s(V_g))\cdot S}{C_{ox}} + \Phi_{ms} + \phi_B - \frac{q_e N_{ox;eff}\cdot S}{C_{ox}} - \frac{q_e N_{it}(\psi_s(V_g))\cdot S}{C_{ox}} \tag{3.37}$$

Where:

$$N_{ox,eff} = \frac{Q_{ox,eff}}{q_e} \tag{3.38}$$

(in cm^{-2}) experimentally obtained

Similarly,

$$N_{it}(\phi_s) = \frac{Q_{it}(\phi_s)}{q_e} \tag{3.39}$$

(in cm^{-2}).

Interface trapped charges $Q_{it}(\psi_s)$ and effective oxide charges $Q_{ox,eff}$ affect the ψ_s-V_g relationship. This implies that reaching typical bias-conditions (accumulation,

depletion or inversion) it will require different gate-voltage values than the ideal case, corresponding to this equation.

Once the $Q_{ox,eff}$ and $Q_{it}(\phi_s)$ were simulated, they could be used to construct the HF-CV curves. In figures 3.5 and 3.6, the HF-CV curves were simulated using the D_{it} from figure 3.3 for p- and n-type silicon respectively and for both sets of equations: exact and closed-form approximation solutions.

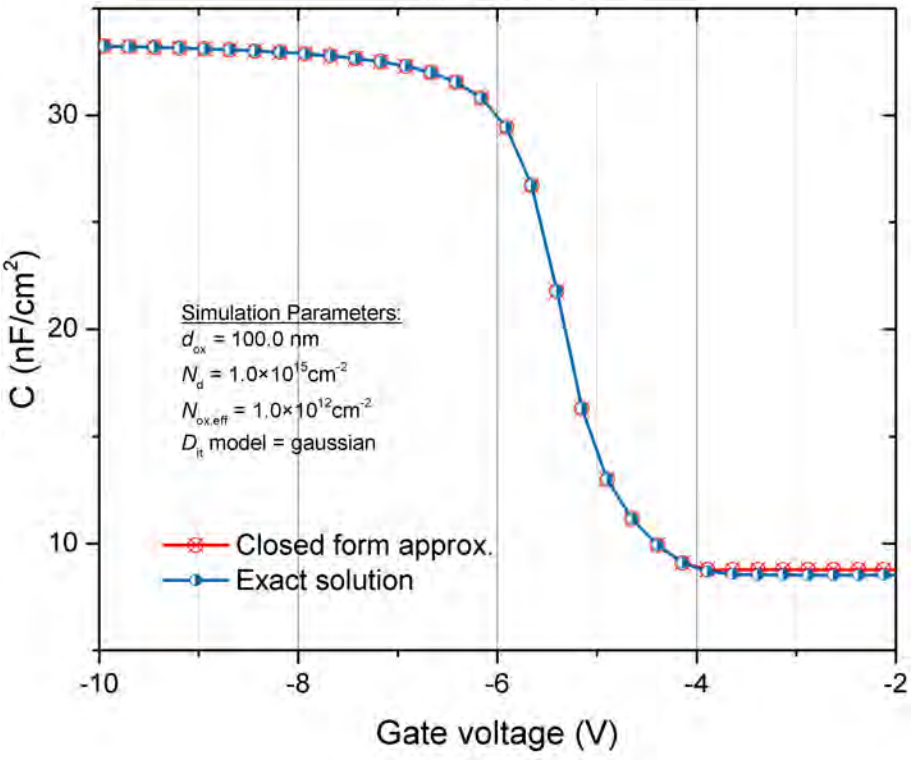

Figure 3.5: HF-CV curves (for p-type c-Si) simulated by the closed-form approximation and the exact solution through the passivation parameters. The D_{it} Gaussian model is used in order to simulate the D_{it} (see figure 3.3).

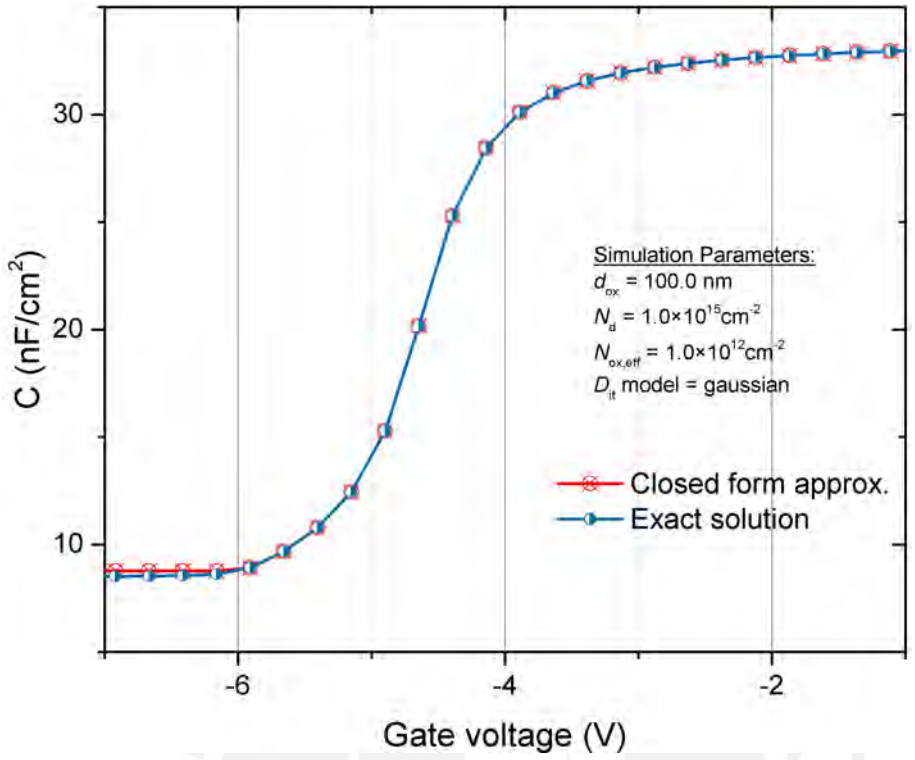

Figure 3.6: HF-CV curves (for n-type c-Si) simulated by the closed-form approximation and the exact solution through the passivation parameters.The D_{it} Gaussian model is used in order to simulate the D_{it} (see figure 3.3).

In order to ease calculation, a constant D_{it} as an approximation was used in different works focused on the midgap D_{it} where recombination rate is highest than at other energy values within the band gap [Gir88; Abe92; Bon17]. This approach was adopted in order to visualize the effect of the passivation parameters on the HF-CV curve as shown in figure 3.7.

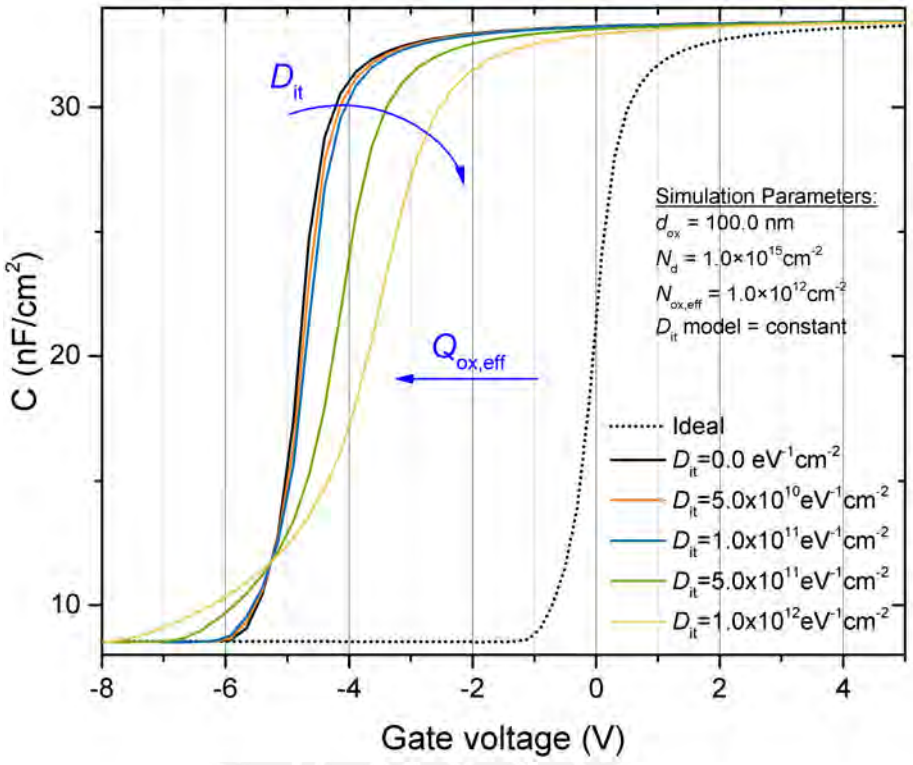

Figure 3.7: The effect of the passivation parameters ($Q_{ox,eff}$ and some values of constant D_{it}s) on HF-CV curves is shown. $Q_{ox,eff}$ produces a shift of the HF-CV curve as seen from equation 2.10. The positive value of the effective oxide charges moves the curve toward the left side. The slope module of the HF-CV curve is inversely proportional to the D_{it}

3.3 Conclusion

In this chapter, some algorithms and mainly an explanation of the equations in which the developed simulation tool is based were discussed.

Two different sets of equations were taken into account in order to construct a HF-CV simulation tool. Before using the sets of equations for the capacitance, the equations which relate the potentials with the charges concentration were presented. First, it is important to construct the dependency between the gate voltage and the band-bending. The capacitance for any set of the equation depends on the band-bending which is related to the surface potential. The ideal case was treated at the beginning, this ideal case or ideal system is defined for an oxide without any charges in the volume and any defect states at the oxide-semiconductor interface. The unique consideration taken into account is the work-function difference factor which depends on the difference between the semiconductor work-function and the metal work-function.

The *closed-form approximation* solution approximates very well to the exact solution almost for all points except for some points at inversion.

For the case when passivation parameters are considered, two models: The Gaussian model and a constant value are taken into account in order to simulate the D_{it} after which is inserted into the Q_{it}. From the simulated D_{it} by the Gaussian model, the Q_{it} was constructed from a general expression derived from geometrical considerations. The general expression of the dependency for V_g and ψ_s considering passivation parameters was used in order to simulate a HF-CV curve which was depicted for both sets of equations and for different doping concentrations.

Finally, through the D_{it} modelled by a constant value, the effect of the D_{it} is shown as well as of the $Q_{ox,eff}$ on the HF-CV curve was shown.

Chapter 4

Experimental data analysis and fits based on SiO_2/c-Si MOS capacitor non-idealities simulations

4.1 Introduction

In this chapter, the capabilities of the simulation tool to deal with experimental data will be tested. The HF-CV simulation tool was presented in the previous chapter.

A thermally grown SiO_2 of 100 nm thickness with subsequently forming gas annealing treatment on n-type crystalline silicon MOS system is analysed. This experimental data comprises HF-CV, transient C-t and ΔC-V measurements [Füs77; Hen11; Töf14; Pre17] for both sweep directions (acc-inv and inv-acc). An appropriated sweep rate is used, it is known as the HF-CV with relaxation measurement in ref. [Hen11] which allows the completion of the generation and recombination of minority charge carries in inversion ti reach stable capacitances as discussed in section 2.1.

The measurements which were measured in both sweep directions allow the analysis of the stability of oxide charges which is widely studied in ref. [Töf14]. The presence of hysteresis indicates that an oxide effective charge is not stable under a bias voltage. Depending on the direction of the hysteresis, two arguments were raised which are

the clock and the counter-clock hysteresis. For n-type (p-type) silicon: The first one (the second one) is associated to charge injection from silicon to the oxide, whereas the second one (the first one) could be explained by two mechanism: injection of charge carriers from the gate contact to the oxide or a mobile charge redistribution depending on the bias voltage such as depicted in figure 4.1.

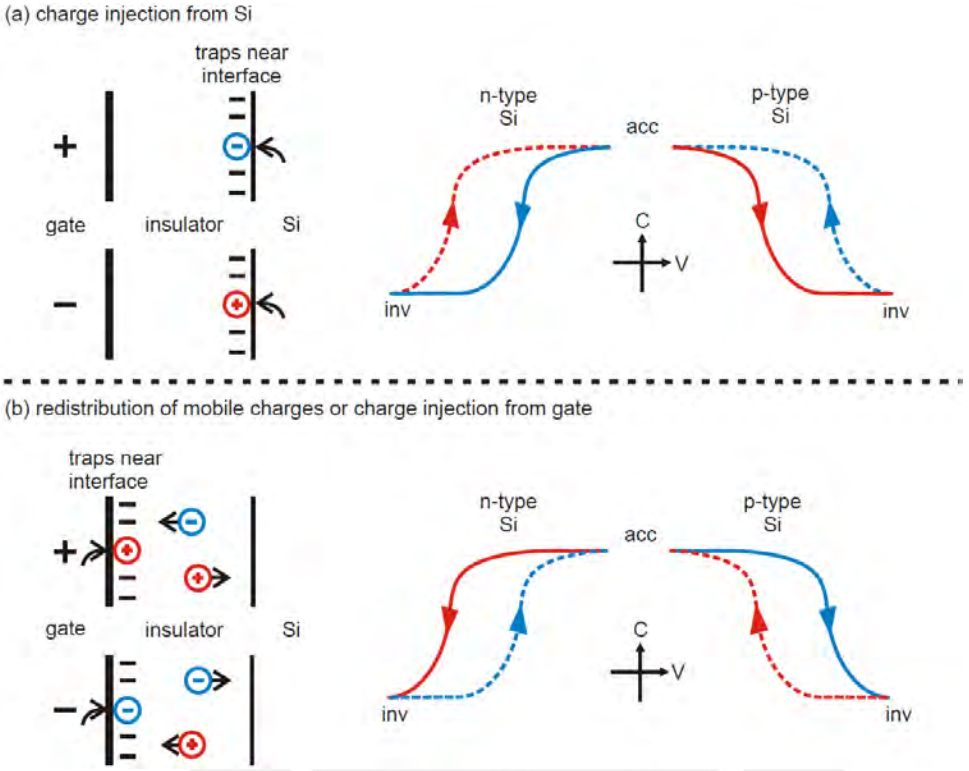

Figure 4.1: Mobile charge injection mechanisms associated to the hysteresis of the HF-CV curves. This figure is taken from ref.[Töf14]. Using the right-hand rule two types of hysteresis are defined: clock and counter-clock hysteresis for each silicon doping type.

The first section will focus on the comparison of the ideal HF-CV curve simulated by the developed simulation tool with the ideal HF-CV curve provided by the HF-CV Messprogramm.

A correction algorithm will be added to the simulation tool in order to evaluate experimental data by calculating the relative error between the ideal curves which were compared in the previous step. Since the HF-CV method is based on the model used, this step allows to reduce the error by the adapted model.

Simulations on passivation parameters based on the experimentally extracted parameters will be performed, then the HF-CV curves will be compared. Finally, the D_{it} will be approximated through simulations of HF-CV curves without prior

information about an extracted D_{it}.

4.2 Simulated ideal HF-CV curves validation

The experimental data of SiO_2/n-type c-Si was analysed. The comparison of the experimental curves in different sweep was performed.

In order to evaluate the model used by the extraction program (HF-CV Messprogramm) with the two equation sets applied in the developed HF-CV simulation tool (the exact and the closed-form approximation solutions), the obtained ideal HF-CV curves must be compared. As a first step, both curves (acc-inv and inv-acc) extracted from the extraction program are represented in figure 4.2.

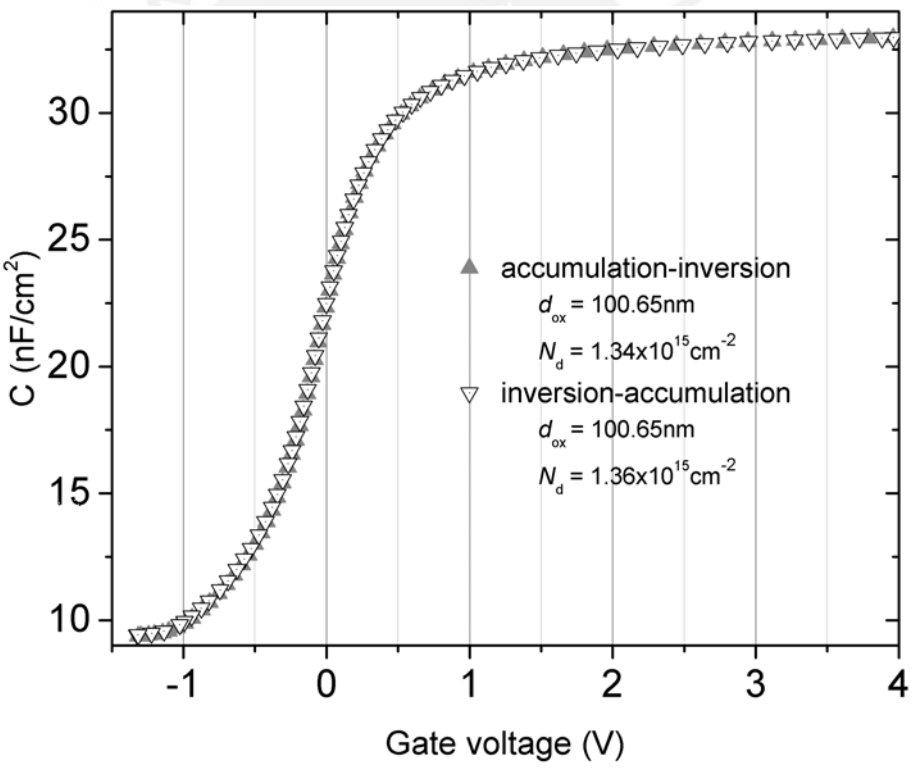

Figure 4.2: The comparison of HF-CV curves calculated by the HF-CV messprogramm assuming ideal MOS in both swepp directions (acc-inv, inv-acc)

The comparison of these curves shows that the oxide thickness extracted by both sweep direction has the same value up to the fifth significant digit (100.65 nm) whereas the dopant concentration up to the second significant digit ($1.3 \times 10^{15}\,\mathrm{cm}^{-2}$). It is worthwhile to remember that these parameters are extracted from the experimental HF-CV curve according to the algorithm described in section 2.2. Since the

change is not very appreciable, fluctuating effects such as charge injection or leakage currents associated with this difference could be neglected. Therefore both curves being similar, and any of them can be chosen. In this work, the ideal HF-CV curve belonging to the acc-inv sweep direction is used.

In order to verify the reliability of the developed tool, the comparison of the two equation sets for an ideal MOS capacitor was performed.

Since the tool includes the constant associated to the SiO_2 layer, the inclusion of two parameters is enough: N_d and d_{ox} which were extracted from the HF-CV measurement (see section 2.2).

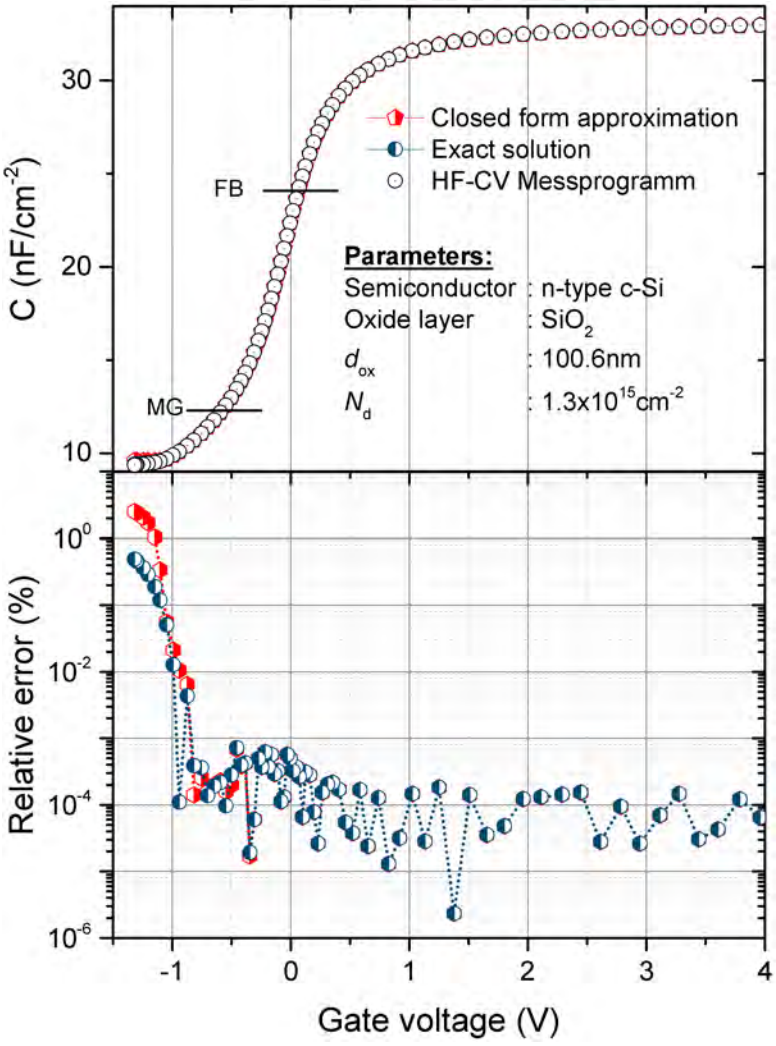

Figure 4.3: SiO_2 ideal curve comparison: the closed-form approximation (enhanced by the Lindner-Fenske Match-point correction [Fen83]) and the exact solution.

Simulations using two different sets of equations were performed: the closed-form approximation with the additional Lindner-Fenske correction, widely recommended

for its simplicity and computationally easier to implement, and the exact solution described in section 3.2.

Looking at the underlying figure, 4.3, the results show a very good approximation with a maximum relative error of around 0.4 % for the exact solution whereas the closed-form approximation presents a maximum relative error of around 2.4 %. Since the exact solution presents the best approximation, it will be taken into account in the results no matter the CPU usage nor other implications.

This comparison will allow to develop a correction algorithm in order to remove the found error related to using different sets of equations. Thus, a better approximation of the simulated HF-CV curve will be obtained no matter the extraction program.

As shown in the previous chapter, the band-bending is an important parameter in order to construct the HF-CV curve. Because it represents the effect of the applied gate-voltage on the semiconductor. It is not possible to measure the band-bending directly, but it could be extracted from the experiment how it will be shown in the following section. Here, the band-bending for the ideal MOS system was simulated. Additionally, in order to evaluate this simulated band-bending, an external program is used. The *Multi-dielectric energy band-diagram* program [Sou06] was used for this purpose.

Since for the ideal curve, the metal-semiconductor work function difference was taken into account, the input parameters for the external program are $W_{ms} + \phi_B$, d_{ox} and N_d extracted from the calculated ideal curve (see figure 4.2).

In addition, this external program allows to simulate the band-diagrams associated to the band-bending. This semiconductor band diagram, although it is simulated for the ideal case, will be valid when passivation parameters are added. Therefore, semiconductor band diagrams for representative points were simulated whereas the metal energy, as well as the oxide energy, are omitted because they change when the passivation parameters are added.

Therefore, it is enough to find a good approximation for the band-bending curve to obtain a simulation of the band diagrams for the ideal system.

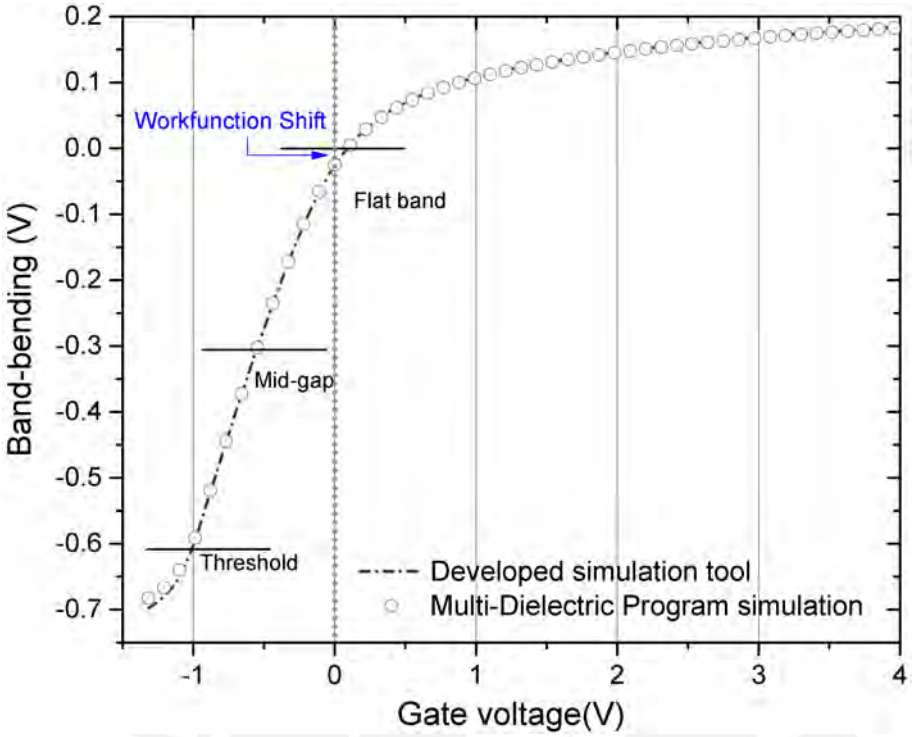

Figure 4.4: The band-bending curve for ideal MOS along with the simulation based on the *Multi-dielectric Band-Diagram* program.

As seen in figure 4.4, a good fitting of the curves was achieved allowing to find approximated band diagrams. Since this graph represents the band-bending caused by a bias voltage. When a voltage is not applied, band-bending must be null (flatband situation), but here a little shift is shown toward the right side, which means there is a remaining band-bending for a zero voltage $V_g = 0\,\mathrm{V}$. This is due to the work-function difference, that introduces an inner potential, which must be overcome in order to reach the flatband situation.

In order to obtain the band diagram, a band-bending shift to the right side means an additional negative voltage would need to be applied. Negative voltage on the gate attracts positive charges in the space charge region. Associated to these positive charges a little negative band-bending corresponds to the zero voltage, according to the potential signs convention [Nic82] a negative potential means band upwards. This is shown in the following band-diagram as depicted in figure 4.5.

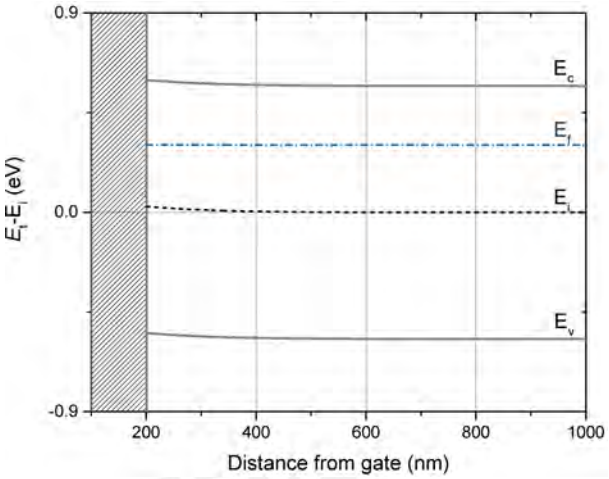

Figure 4.5: Zero voltage SiO_2 band-diagram simulation using the *Multi-Dielectric Band-Diagram* program.

In figure 4.6 the most representative band-diagrams was simulated:

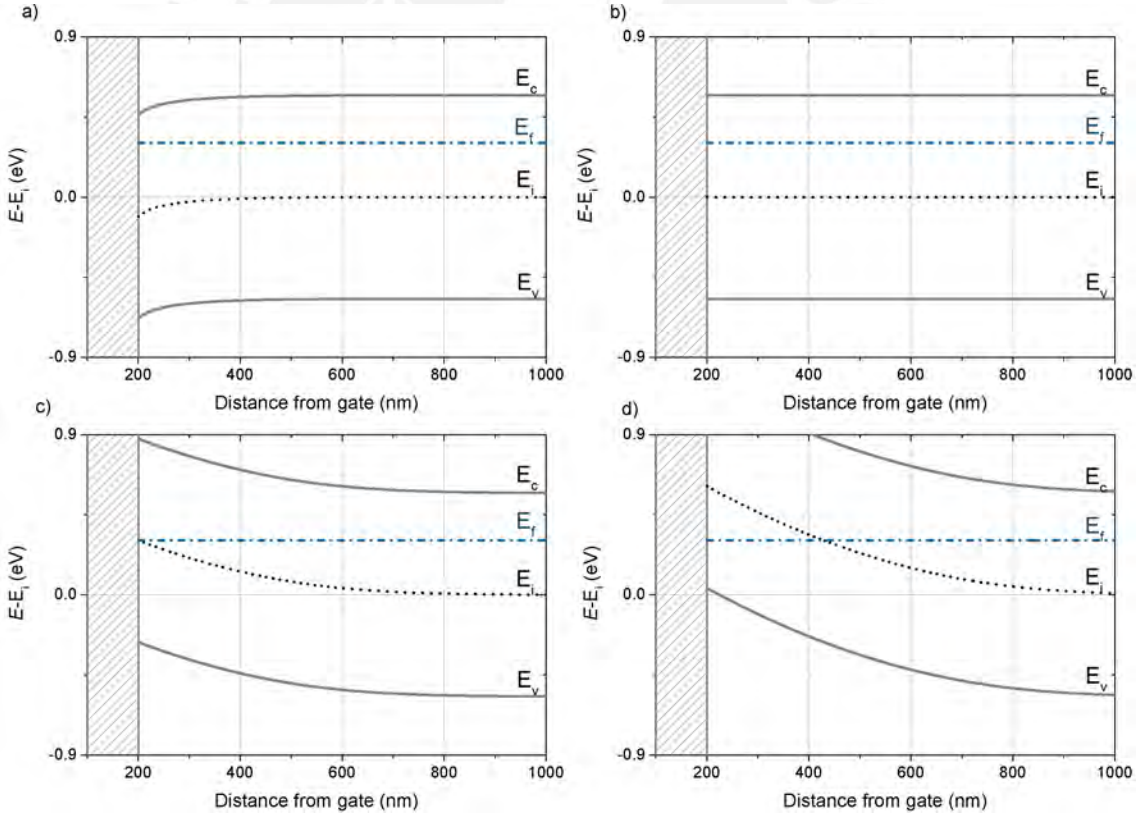

Figure 4.6: a) Accumulation bias condition: For an arbitrary voltage, for example $V_g = 1.000\,\mathrm{V}$, b) Flatband voltage: According to *Multi-Dielectric* program $V_g^{FB} = 0.089\,\mathrm{V}$ which is the same value for the simulation, c) Midgap voltage: In this case, it is replaced by the simulated value $V_g^{MG} = -0.550\,\mathrm{V}$, d) Threshold voltage: Corresponding to a value around $V_g^{TH} = -1.000\,\mathrm{V}$.

4.3 Simulated Nonidealities HF-CV curves validation: Simulated and experimental curves comparison

In section 4.1, concepts about oxide charge stability were discussed. These concepts will be used now in order to test the reliability of the experimental data. The HF-CV curves were measured in both sweep directions (acc-inv and inv-acc) along with the transient C-t curves and $\Delta C - V$ curves as shown in figure 4.7.

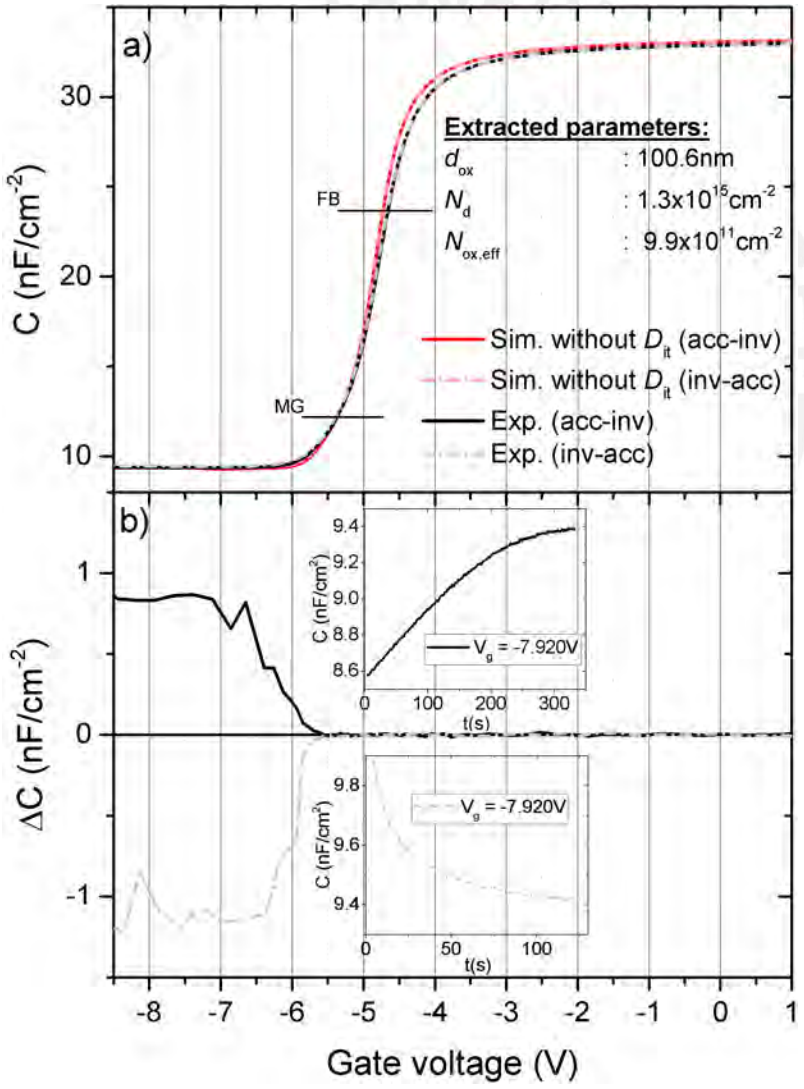

Figure 4.7: Charge stability analysis of SiO_2.

From c-t curves, the extraction program constructs ΔC-V diagram which is related to R-G rates of charge carriers as commented earlier (sections 2.1 and 2.2.1).

In accumulation, due to the gate voltage value, the majority charge carriers are attracted to the interface, the small-signal is in charge of fluctuating them. During the positive part of the AC small-signal, the majority carriers come from the bulk (rarely from the rear contact) to compensate this perturbation (since concentrations of majority carriers are very high this compensation is immediately reached). During the negative part, the majority charge carriers are delivered to the quasi-neutral region in the semiconductor bulk. In this situation, the R-G rate has two contributions which are thermal effect and by bulk defects, but the thermal R-G rate is largely dominant in comparison with the related to bulk defects. Therefore, when measuring capacitance as a function of time for a specific voltage step, the capacitance must remain constant in time. When ΔC-V is constructed $\Delta C = C_{t_f} - C_{t_0}$ is calculated (where t_f means time at the end, and t_0 means initial time). Since C in accumulation is independent on the time, ΔC must be zero. This is observed in figure 4.7b).

In Depletion, there is a reduction of the majority charge carriers, but ionized dopants increases and contribute with the total charges, the response of charges remains constant ($C(t) = constant$) for each voltage step.

When majority charge carriers are depleted, the number of minority charge carriers increases. Since the thermal R-G rate, in this case, is very small in comparison with majority charge carriers, the R-G rate is dominated in this case by bulk defects (it is important to take this into account). The R-G rate decreases substantially, hence a longer period of time is required in order to compensate charge displacements. As described in section 3.2 the minority charge carriers only fluctuate around the same density and capacitance remains constant for the subsequent voltage steps in inversion. In order to reach this condition a characteristic time is required for each voltage step. This time is known as the *relaxation time*. Therefore $C(t) \neq constant$ and depends on the sweep direction. For example, measuring from accumulation to inversion, once charges are in a stationary condition, in order to reach the next voltage step, it requires to add minority charge carriers to the inversion layer (a thin layer formed by minority charge carrier close to the interface), then the minority charge carriers need to be generated. Therefore, the C-t curve, in this case, increases monotonically how is depicted inside the adjacent figure. When C-t is measured from inversion to accumulation, a counter mechanism is given and this one is associated with a recombination process and the C-t curve looks like a monotone decreasing function, thus $\Delta C \neq 0$ and since generation or recombination rate increases, ΔC

increases (acc-inv) or decreases (inv-acc) as well [Füs77; Nic82; Pie95; Vas08; Pop10; Hen11; Töf14].

The HF-CV Messprogramm is prepared to measure these curves, the algorithm waits a specific time (by default 10 seconds) when the stationary condition is reached. If something is wrong (if the model assumptions are not fulfilled by non-contemplated effects) a deep analysis is necessary to do and now, with the developed tool is possible to add a new way to evaluate them.

It is noticed the sample studied fulfils with the MOS model assumptions in a good approximation. The effects such as leakage currents and instabilities by charge injection or redistribution are neglected. The comparison of the simulated HF-CV curve without D_{it} and the experimental curve indicates the existence of trapped charges at the interface (see figure 4.7).

The D_{it} was extracted from the experimental curve as described in section 2.2.1 and the Gaussian model (see section 3.2) was used in order to fit the experimentally extracted D_{it}. As depicted in figure 4.8, the fitting of different parameters was tested.

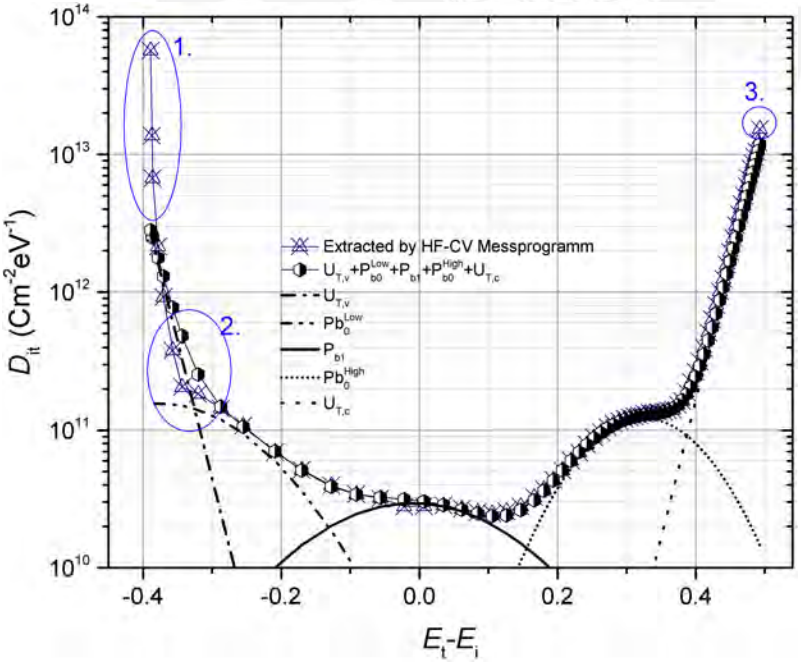

Figure 4.8: The Gaussian model fitting over the experimentally extracted D_{it} along with each defect type contribution. The circles represent parts where the model does not fit the experimentally extracted D_{it}.

The fitting parameters are depicted in the table 4.1 which takes into account the

D_{it} fitting parameters			
Dangling bond	$N_t^{P_{b0L}}$, $N_t^{P_1}$, $N_t^{P_{b0H}}$ (cm^{-2})	w_L, w_1, w_H (eV)	E_{0L}, E_1, E_{0H} (eV)
P_{b0}^L	4.7×10^{10}	0.24	-0.375
P_{b1}	1.0×10^{10}	0.27	-0.010
P_{b0}^H	2.5×10^{10}	0.16	0.325
Strained bond	N_v, N_c (cm^{-2})	β_v, β_c (eV^{-1})	E_v, E_c (eV)
$U_{T,v}$	7.0×10^{15}	46	-0.56
$U_{T,c}$	2.6×10^{14}	46	0.56

Table 4.1: Fitting parameters based on the Gaussian model.

fitting restrictions discussed in section 3.2.

The charge densities per unit area could give some ideas about the HF-CV curve construction. Using the experimentally extracted D_{it} and based on the method explained in section 3.2 the density of trapped charges Q_{it} can be constructed. Thus, in figure 4.9, a comparison of charge densities is depicted.

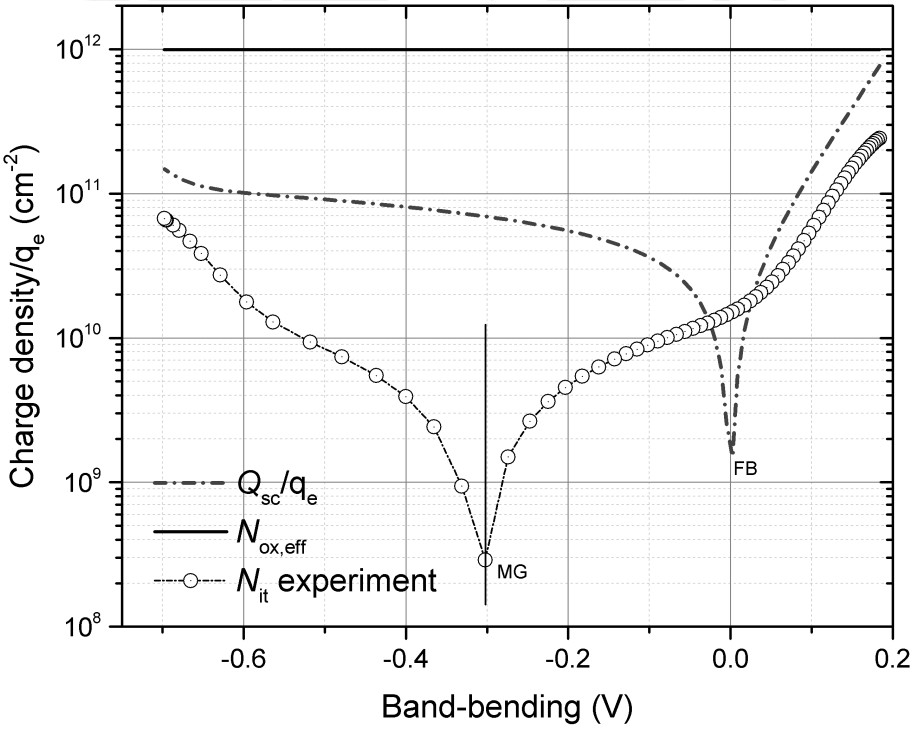

Figure 4.9: The comparison of relevant steady-state charge densities in function of the band-bending. At midgap Q_{it} practically does not affect Q_{sc} whereas its largest contribution is given at the flatband. Since $Q_{ox,eff}$ is constant for all ψ_s, its contribution is the same for each point.

At midgap, N_{it} curve reaches its minimum value, because the positive and negative interface trapped charges are almost each other compensated. This diagram gives

an important reason why $N_{ox,eff}$ at midgap is chosen as a simulation parameter instead of the $N_{ox,eff}$ at flatband, it justifies the topic assumed in section 2.2.1.

In addition, from equation 3.37, it is possible to construct the band-bending as a function of the gate voltage. A comparison between the experimentally constructed and the simulated band-bending is performed as shown in figure 4.10.

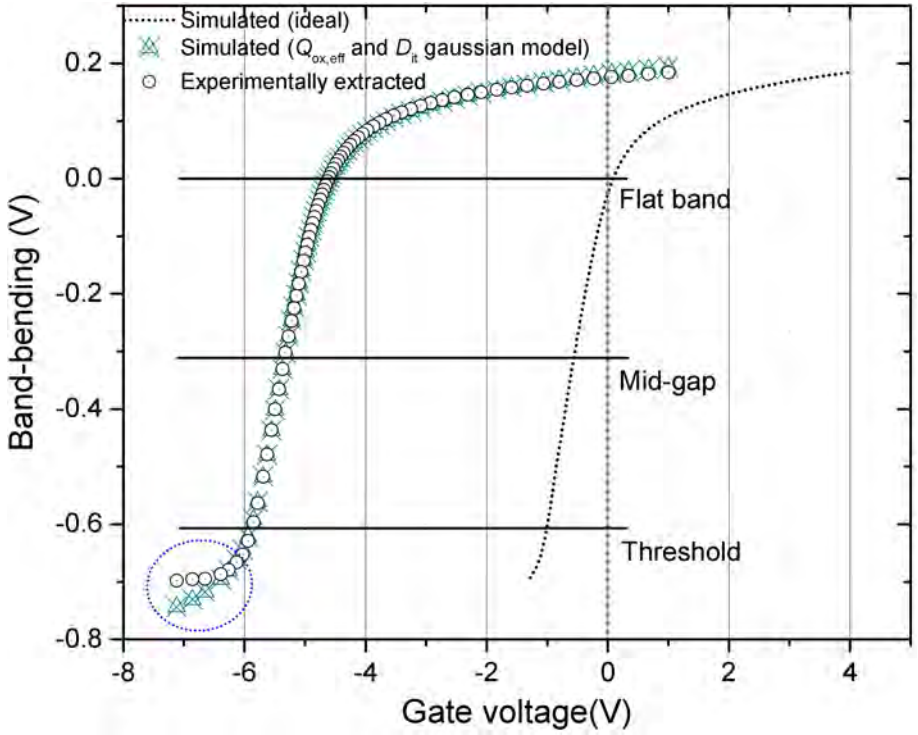

Figure 4.10: The simulated and experimentally constructed band-bending are compared. Inside the circle, the points do not fit in the simulation are shown. An error contribution is given by the used model, but this error is witnessed in inversion when the largest difference is given.

The band-bending presents a deviation in inversion. This deviation could also contribute to an increase of the error found in the HF-CV curve.

In section 4.2 the ideal curve simulation was analysed and compared with the extracted ideal one. The solution through exact equations presented a low relative error (modelling error). When passivation parameters are introduced, this error remains present as a background. In order to remove this modelling error, a solution is proposed as follows.

Once the capacitance is simulated for a voltage step $C_{simulated}$, an additional modelling error is incorporated. This additional capacitance depends on whether this capacitance is above or below the corrected capacitance value $C_{corrected}$. Since the

extraction algorithm constructs the ideal curve for each voltage step, i.e. for each $C_{experimental}$ (experimental capacitance) there is a correspondent $C_{ideal\ extracted}$. Thus, it is possible to simulate a HF-CV curve through passivation parameters along with its ideal curve $C_{ideal\ simulated}$. This simulated ideal curve is compared with the extracted curve, a factor is defined so that, if the $C_{ideal\ simulated}$ is below the $C_{ideal\ extracted}$, the factor takes the value of 1 in order to compensate the missing capacitance, if they are the same, the factor is zero and if the simulated curve is above the extracted one, the factor takes the value of -1. Thus, through this algorithm, the remaining capacitance could be removed.

$$C_{corrected} = C_{simulated} + factor \times |(C_{ideal\ extracted} - C_{ideal\ simulated})| \tag{4.1}$$

where:

$$factor = \begin{cases} 1, & \text{if } (C_{ideal\ extracted} - C_{ideal\ simulated}) > 0. \\ 0, & \text{if } (C_{ideal\ extracted} - C_{ideal\ simulated}) = 0. \\ -1, & \text{otherwise.} \end{cases} \tag{4.2}$$

This correction method must be used only in the case where the extracted ideal curve is reliable according to the considerations exposed in sections 2.2.1 and 4.1.

From the fitted D_{it} in figure 4.8, the Gaussian Model is composed of functions associated with each defect type. The total D_{it} is composed by the total sum of these functions (eq. 3.33). In figure 4.11, the contribution of each function to the total D_{it} through the comparison of the HF-CV curves is shown.

An analysis can be done in figure 4.11. First, the last points in the left side (inversion) can be interpreted as error-independent from the associated defect function. Comparing the number of points for the ideal and the experimental curves (it can be seen from the band-bending graph in figure 4.4). Some points in the ideal curve are omitted or not calculated by the HF-CV Messprogramm. Then, these points in inversion are not corrected, therefore the modelling error is superposed to the D_{it} modelling error, doing the relative error almost the same for all cases.

A pronounced peak close to the flatband point is also observed. This could be due to the maximum effect of trapped charges is given at this point according to figure 4.9. At midgap, the relative error decreases significantly since at this point Q_{it} takes

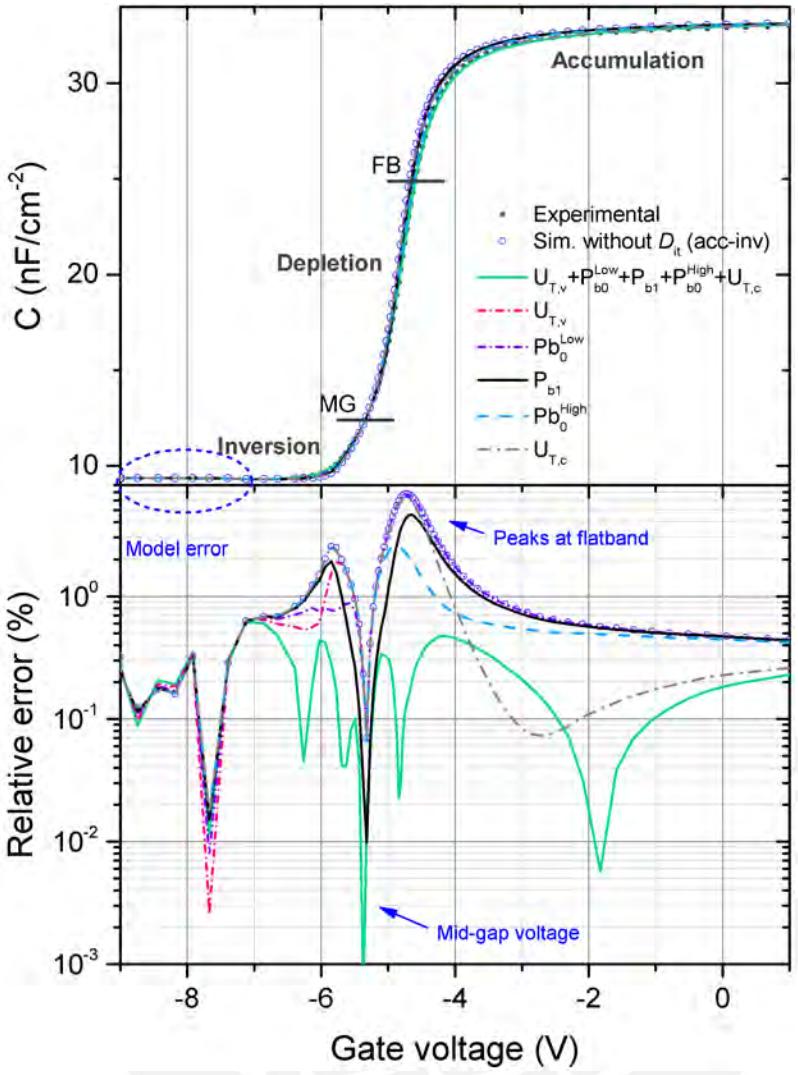

Figure 4.11: The comparison between the experimental and the simulated HF-CV curves based on each defect type contribution $U_{T,v}$,P_{b0}^{Low},P_{b1},P_{b0}^{High},$U_{T,c}$ and the total sum according to the Gaussian model

its minimum value.

Comparing the HF-CV curves related to the extreme functions $U_{T,v}$ and $U_{T,c}$, they contribute to the fit in inversion and accumulation respectively which makes to decrease the relative error significantly when P_{b0}^{High} is added. The curve made up by the total sum of defect functions changes its slope and a part of the curve could pass toward the right side. This means the slope module decreases due to the addition of the defect functions and for some points, it could be even more than what is needed.

When P_{b0}^{Low} is added to $U_{T,v}$, the effect of both functions makes decrease significantly the error in the total sum. P_{b1} has an effect around the central points of the HF-CV curve, in depletion principally. Tiny displacements from the midgap occur because

of tiny displacements of the Q_{it} at midgap, since at this point although is minimum, its effect is not totally neglected.

Usually, a single state at midgap is taken as a reference for comparing different D_{it} curves because recombination at this point has the maximum effectiveness. In this part, three different models will be used, one of them is a single state at midgap, represented by a constant function, in order to compare its effects on the simulated HF-CV curve.

The D_{it} at midgap has the value of $2.48 \times 10^{10}\,\mathrm{cm}^{-2}\,\mathrm{eV}^{-1}$, based on this information an U-shape model was constructed replacing the gaussian functions by this D_{it} value, keeping the exponential functions ($U_{T,v}$ and $U_{T,c}$) from the Gaussian model as shown in equation 3.34.

The different simulated D_{it}s along with their HF-CV curves and the relative error associated to them are depicted in figure 4.12.

It is observed that the Gaussian model has the best approximation compared with the other models because the Gaussian model has more functions that contribute a better fitting of the experimentally extracted D_{it}. The constant D_{it} presents the largest relative error. In figure 4.12, as the above figure (see figure 4.11), endpoints at left side are not corrected by the modelling error correction algorithm.

Therefore, considering a single state at midgap with the tail exponential functions (the U-shape model) for fitting a D_{it} produces a large error. A question raised at this point is, what would be the effective single state which would reproduce with the minimum error of the HF-CV curve? This question is difficult to answer because the states at midgap have the most effective recombination and then the states around midgap decrease until a certain point where the recombination effectiveness is low as discussed in section 1.2. A more representative value must produce a closer HF-CV curve taking into account the most recombination effectiveness states, which lie around the midgap. In the following section, it will try to answer this question.

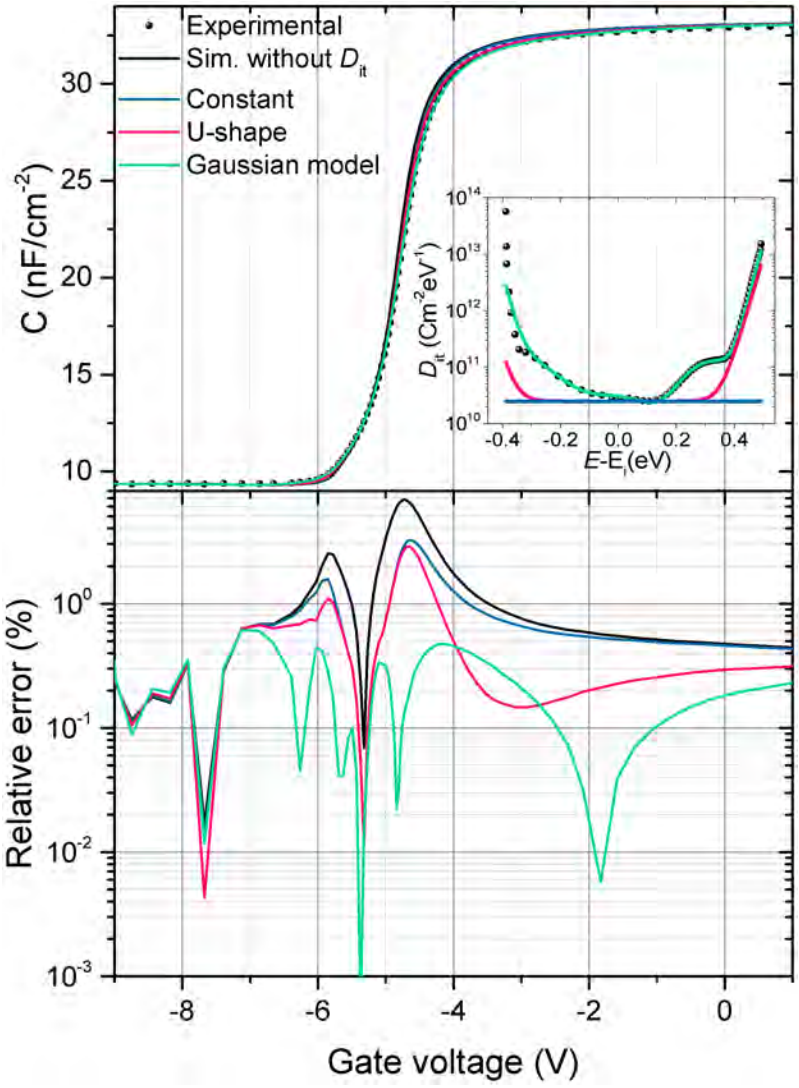

Figure 4.12: HF-CV curves based on different D_{it} models. Each D_{it} was simulated taking into account the obtained D_{it} at midgap.

4.4 D_{it} fitting based on an U-shape model through HF-CV characteristic simulations

The equation 3.35 states Q_{it} is obtained by integrating the D_{it} function with its respective occupation probability. The total derivative of Q_{it} is proportional to the D_{it} according with [Nic82]:

$$\frac{dQ_{it}(\psi_s)}{d\psi_s} = -\frac{1}{q_e} \cdot D_{it}(\phi_s) \tag{4.3}$$

If it is considered D_{it}^1 and D_{it}^2, two D_{it}s functions, so that from the integral 3.35, $Q_{it}^1 = Q_{it}^2$ is obtained. Equation 4.3 states that an unique solution exists so that $D_{it}^1 = D_{it}^2$. Therefore, any modelled D_{it} is an approximation of an unique D_{it}.

On the basis of the experimental HF-CV curve, a test D_{it} could be used for simulating a HF-CV curve and this D_{it} would be an approximation and the HF-CV curve would have a specific relative error when is compared with the experimental curve. If several test D_{it}s are tested for HF-CV curves each D_{it} would represent an approximation of the real D_{it}, and in order to compare the approximation, the mean square error (MSE) for the associated HF-CV curve would be a method for comparing each of them objectively.

The most accurate D_{it} would be the one with the least MSE of the HF-CV curve. In this case, MSE is taken into account because it represents the total sum of squared errors of a curve which due to being squared is positive and would allow a better comparison of the total error of a curve.

Using the U-shape model, a method to fit a D_{it} based on fitting of HF-CV curves will be tested. From the equation 3.34, the U-shape parameters are reduced to only three which are the amplitude of the exponential functions N_v, N_c and the constant D_{it}^0. $\beta_v = \beta_c = 40\,\mathrm{eV}^{-1}$ from experimental results [Fli95] and for the energetic position is assumed the values of $E_v = -0.56\,\mathrm{eV}$ and $E_c = 0.56\,\mathrm{eV}$.

Since the range of these parameters does not change dramatically and the slope in the principal part of the curve depends on the values around the midgap (see the change of the slope in function of a single surface state in figure 3.7) then, the fitting will depend principally on D_{it}^0 and it could be assumed a tiny range for each parameter in order to fit the HF-CV curve. When Q_{it} is constructed, the degeneracy

factor for the Fermi function in equation 3.35 presented in section 3.2 is taken into account and the correction modelling error algorithm was also used.

As a first step, it is assumed a range for the U-shape parameters where the solution could be found, thus:

$$\begin{cases} D^0_{it,i} \leq i \leq D^0_{it,f} \\ N^i_c \leq j \leq N^f_c \\ N^i_v \leq k \leq N^f_v \end{cases} \tag{4.4}$$

A fitting method for the non-linear system is needed, but in order to follow each step of the fitting, a slow algorithm will be used.

The combinatorial product of the possible parameter sets is made in order to have the maximum of possibilities and the HF-CV curve is calculated for each case, so that:

$$MSE = S_{i,j,k} = \sum_{m=1}^{M} e_m^2 = \sum_{m=1}^{M} \left(C_m^{exp} - C_m^{sim} \left(V_{g,m}; D^0_{it,i}, N_{c,j}, N_{v,k} \right) \right)^2 \tag{4.5}$$

Where, there are M experimental points for each curve.

From the experimental data, and using the following ranges: $4.52\,\text{eV} \leq i \leq 4.64\,\text{eV}$, $1.2 \times 10^{14}\,\text{cm}^{-2} \leq j \leq 3.0 \times 10^{14}\,\text{cm}^{-2}$ and $9.0 \times 10^{14}\,\text{cm}^{-2} \leq k \leq 1.8 \times 10^{15}\,\text{cm}^{-2}$.

The choice of these ranges was carefully tested. First, only the range of i parameter was tested because the HF-CV curve is more sensitive to its changes. Then the other ranges related to the other parameters will be tested until they reach a very short length. This is made only in order to reduce the ranges, it is possible to use larger ranges but the CPU usage would be larger.

Once the ranges are selected, a number of the possible value of the parameters is taken, in this case, they were 20 points for each parameter. Then the combinatorial product of these parameters produced 8000 possible cases, where each case N is defined by a triplet (i, j, k).

$S_{i,j,k} = S_N$ is saved in a list of values, as is depicted in figure 4.13 (here, only some points from the total possible values are shown). Finally, from the minimum value of S_N, the parameters i,j and k that are close to the optimized parameter values

are extracted.

The more points are taken for the ranges, the more close are the found parameters to the optimized ones. Each point in the graph represents a S_N, only the values close to the minimum are depicted because the other points are too far from this value.

This fitting process belongs to the non-linear solutions (unlike a linear regression), the conventional method is based on the $\xi^2 = S_N$ minimization, but since the curve to be optimized is non-convex, the optimization could not be reached by the Fermat's Theorem. In this sense, by this method, an approximation to the solution is achieved.

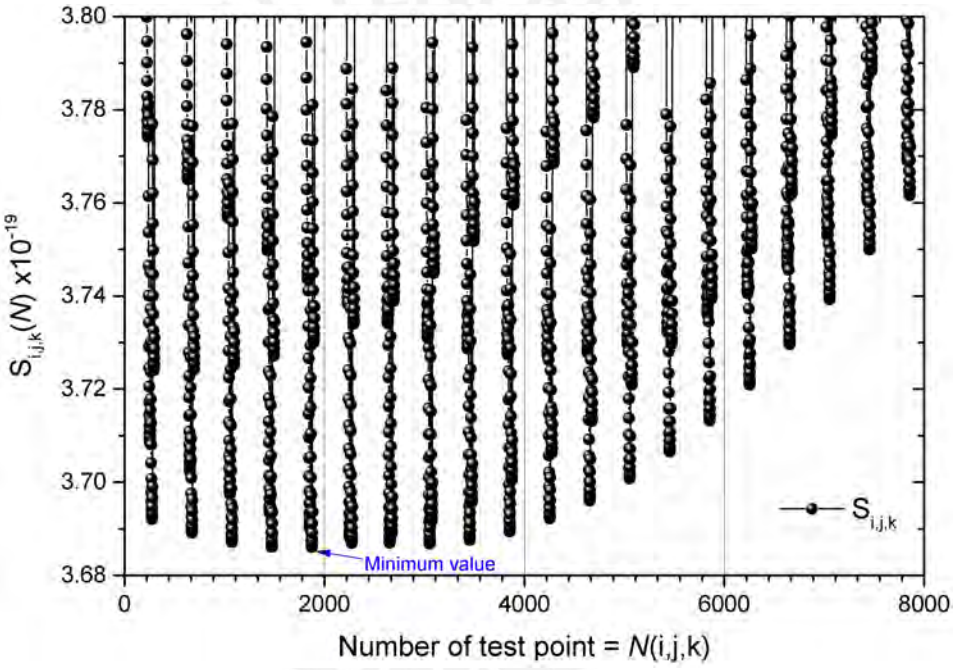

Figure 4.13: The Mean Square Error for a range of combinatorial product of possible optimized parameters ($D_{it}^0 = i, N_c = j, N_v = k$) from the D_{it} U-shape model (see section 3.2). The minimum value of the discrete function $S_{i,j,k}$ represents an approximation to the absolute minimum of a continuum function.

From the minimum MSE for the simulated HF-CV curves, the following parameters are obtained $D_{it}^0 = 4.54 \times 10^{10}\,\mathrm{cm}^{-2}\,\mathrm{eV}^{-1}$, $N_c = 2.43 \times 10^{14}\,\mathrm{cm}^{-2}\,\mathrm{eV}^{-1}$ and $N_v = 1.51 \times 10^{15}\,\mathrm{cm}^{-2}\,\mathrm{eV}^{-1}$.

The comparison between the fitted and the experimental HF-CV curves are depicted in figure 4.14. An error of less than 1 % is reached and the last eight points in inversion are not corrected similarly to figure 4.11. From these points, the algorithm developed fits them but despite the relative error is not appreciable, there is an

additional error due to using different models (for the extraction and for simulating them), this conducts to an error for the parameters instead of the HF-CV curve. Therefore, at these points, more error will be added in the Q_{it} and its respective D_{it}.

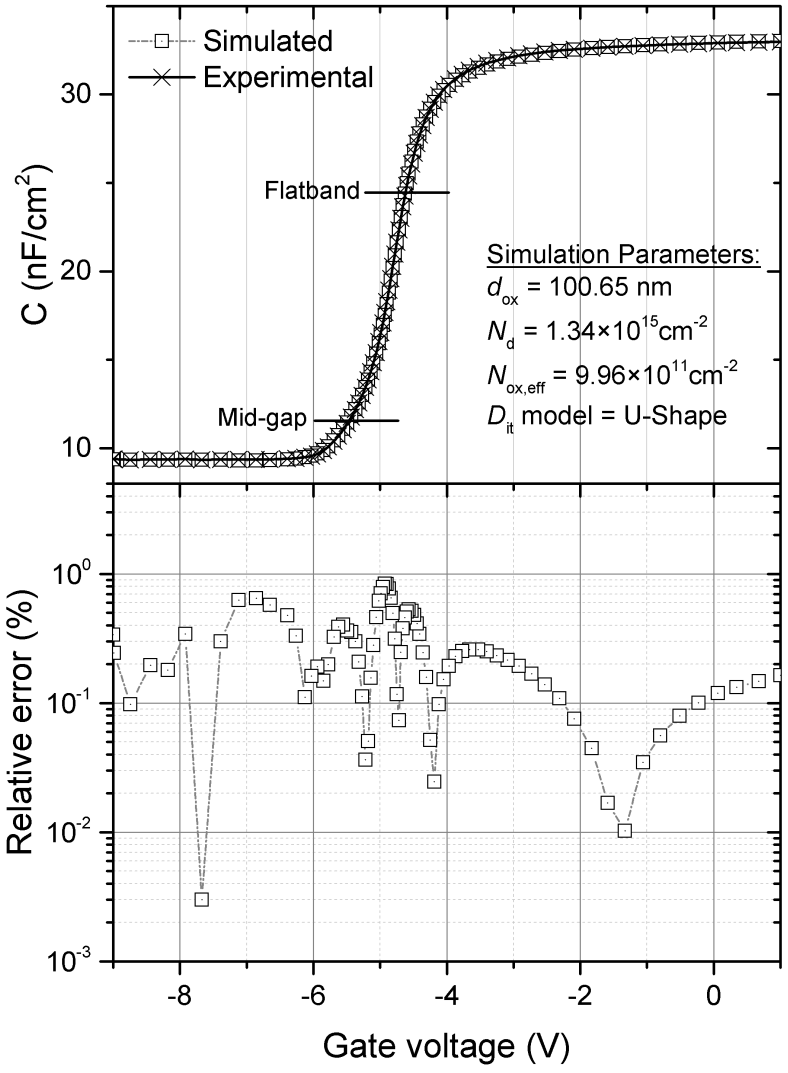

Figure 4.14: This figure depicts relative error of the fitted curve. In this case, degeneracy factor of the Fermi function was considered.

The corresponding Q_{it} is represented in figure 4.15 along with the constructed one from the experimentally extracted D_{it}. Since the approximate Q_{it} considers a simple U-shape model, the comparison is made by the average values calculated by equation 4.6.

$$\overline{Q}_{it} = \frac{1}{\phi_s^f - \phi_s^i} \cdot \int_{\phi_s^i}^{\phi_s^f} Q_{it}(\phi_s) d\phi_s \tag{4.6}$$

On the left side, there is an additional error due to the used model as described in the previous graphic. The Q_{it} average has a similar value until the first significant digit.

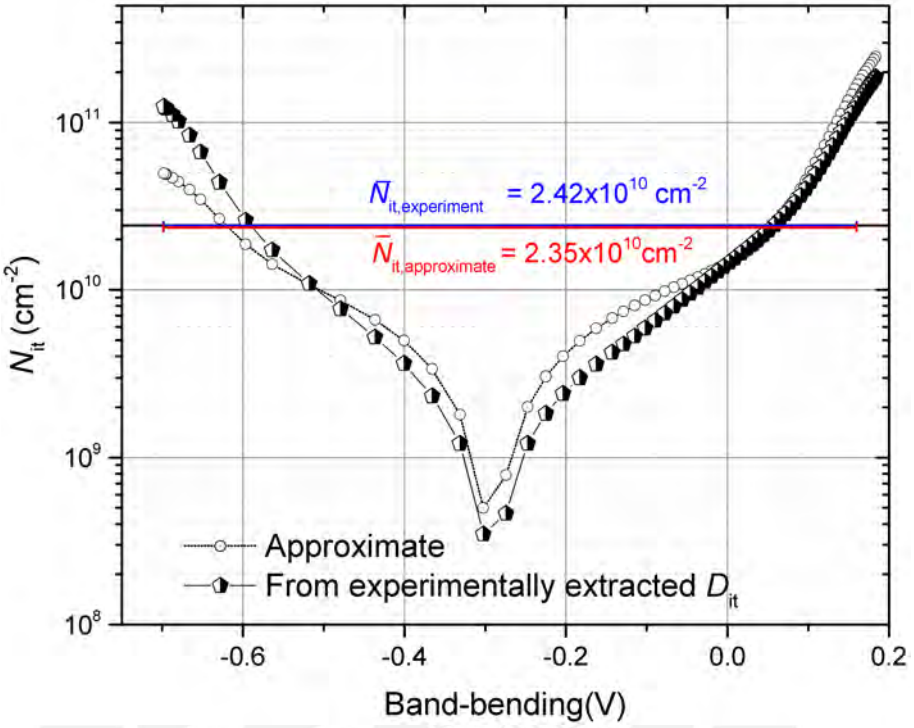

Figure 4.15: From the last figure, $Q_{it}(\psi_s)$ was extracted. Average value is closer to the experimental one showing that the effect of trapped charge at the interface is approximated to the experiment.

The D_{it} is extracted from the fitted HF-CV curve. Hence, this D_{it} represents a fitted D_{it} based on the experimental HF-CV curve. Comparison between both D_{it}s are depicted in figure 4.16. As in the previous case, an modelling error is added to the left side for the last eight points corresponding to the points in inversion. The use of a U-shape model is supported by the empirical description in reference [Fli95], which is related to the *intrinsic distribution* because of the close relation with the pure silicon bonds. Average D_{it} is calculated by the equation 4.7.

$$\overline{D}_{it} = \frac{1}{\phi_s^f - \phi_s^i} \cdot \int_{\phi_s^i}^{\phi_s^f} D_{it}(\phi_s) d\phi_s \tag{4.7}$$

From the constant function belonging to the considered U-shape model could obtain an interpretation. Calculating the average of central values (between -0.25 and $0.25\,\mathrm{eV}$) from the experimentally extracted D_{it}, this value is approximated to the constant function, which is $0.43\,\mathrm{eV}$ whereas the found constant function

$D_{it}^{0} = 0.45\,\text{eV}$. From the reference [Bla16], the deep states whose interface state recombination is greater than 90 % of the midgap value depends, in the simplified case or for limiting cases, on doping concentration, level injection and the oxide fixed charges. This range could take the value of 0.7 eV. In the present work is not possible to establish exactly until which value of energy the recombination is greater than 90 % of the midgap value but usually is similar in comparison with the considered energy range. Thus, this constant value could be represented as a state values average for which recombination is very significant.

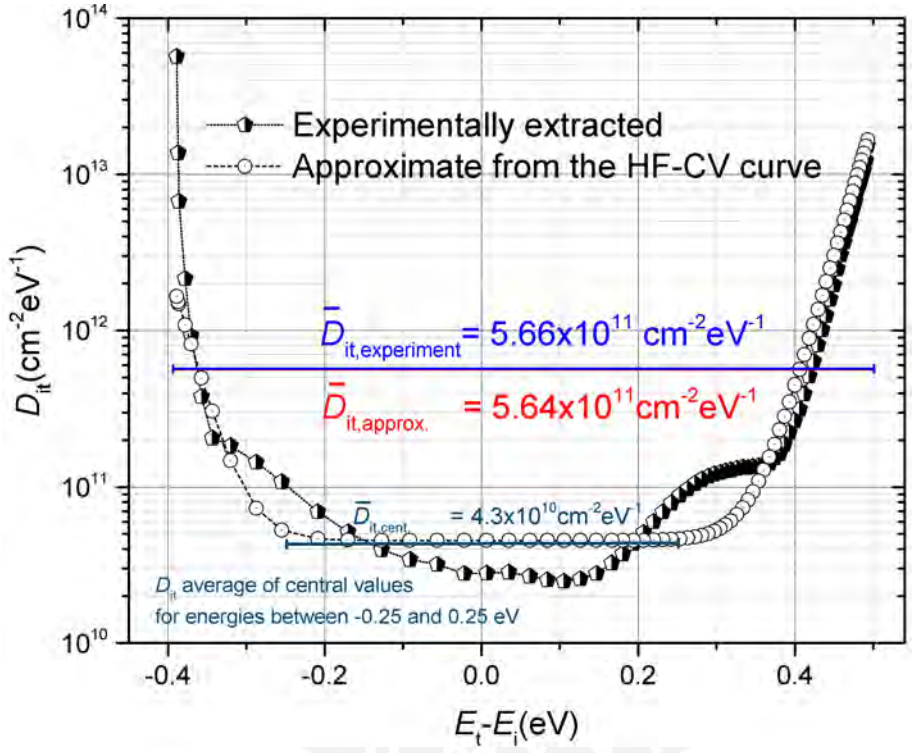

Figure 4.16: The comparison of experimentally extracted and approximate by simulations of the HF-CV curves D_{it}s. The average value calculating according to equation 4.7 has a relative error around 0.35 %. In addition the constant function in the U-shape model could be interpreted as an average of central values of the experimentally extracted D_{it}, in this case for energies between -0.25 and 0.25 eV.

4.5 Conclusion

In this chapter, the program presented in chapter 3 was validated by experimental data.

The extraction program allows to calculate the ideal curve, i.e. the HF-CV curve with $D_{it} = 0$ and $Q_{ox} = 0$ associated with the studied MOS system. In the first part, the ideal curve associated with the extraction process was compared with the simulated one, obtaining a better approximation with the exact solution in comparison with the *closed-form approximation*. The associated band-bending for the ideal case was validated by the *Multi-dielectric Band-Diagram* program, which allows to simulate band diagrams for this MOS ideal system.

In section 4.3, the experimental HF-CV data of thermal SiO_2/c-Si MOS device was used to validate the developed simulation tool. The sample presents a good stability of charges which allows to select any of the two measured curves (acc-inv or inv-acc) since the hysteresis is neglectable and both can be seen as equivalent. The HF-CV curve for the acc-inv sweep direction was chosen.

The experimentally extracted D_{it} is fitted through the Gaussian model and using the algorithm presented in the previous chapter, the corresponding HF-CV curve is constructed. A correction algorithm is added in order to remove the modelling error because the set of equations considered by the extraction program is different from the exact and the closed-form approximation. Each defect function was evaluated in order to compare its effect on the HF-CV curve. Then, on the basis of three different models: Gaussian, U- shape and a single state (or constant function) models, the D_{it} was simulated. The experimentally extracted D_{it} value at midgap was considered for each simulation.

A comparison of the resulting HF-CV curves showed that the belonging one to the Gaussian model presents the lowest relative error while the single state model presents the largest relative error.

In section 4.4, through a D_{it} model, a way to obtain an approximation of the D_{it} from the experimental HF-CV curve is proposed. The algorithm is relatively simple because of the interest in evaluating each step, regardless of the time consumed by the program. Based on the mean squared error (MSE) the algorithm approximates the HF-CV curve which has the minimum MSE. Finally, the obtained D_{it} curve,

based on the U-shape model, is compared with the experimentally extracted one. Different interpretations of this resulting D_{it} were discussed.

Chapter 5

Summary and outlook

A simulation tool of High-Frequency Capacitance-Voltage (HF-CV) curves based on passivation parameters was developed and validated using experimental data. Different aspects concerning the passivation parameters (Q_{ox} and D_{it}) were discussed and a suitable, relatively simple way of fitting the D_{it} based on a D_{it} U-shape model as well as the experimental HF-CV curves was proposed. The code developed for this tool is publicly accessible to the community in GitHub (Migusb).

High-Frequency Capacitance-Voltage simulation for different passivation parameters

Based on the exact and the *closed-form approximation* solutions describing a MOS capacitor, a tool was developed to simulate HF-CV curves based on different passivation parameters. The effects of these parameters on the HF-CV curve were discussed and are in accordance with previously published results in the scientific community.

On the one hand, an ideal MOS system was defined as one that shows an absence of the oxide charge density (Q_{ox}) and the interface trap density (D_{it}). The effect considered was the metal-semiconductor work-function difference (W_{ms}). On the other hand, the passivation parameters were considered as a non-idealities of the system. The simulated band-bending was compared and in accordance with the one resulting from the *Multi-Dielectric Band-Diagram* program.

The effect of both non-idealities, D_{it} and $Q_{ox,eff}$, was analysed by simulating their

effect on the calculated HF-CV curve. Since the D_{it} is a function which depends on the energy, three different models were presented: (1) The Gaussian model composed by a sum of two exponential functions for the band tails and three Gaussian distributions related to the defects centers at the SiO_2/c-Si interface, (2) the U-shape model made up by the two exponentials functions along with a constant value D_{it}^0 which defines the D_{it} at the midgap and replaces the Gaussian distributions of the defined Gaussian model and (3) The representation by a single state or a constant function model based on the D_{it} at the midgap. The expression for the interface trapped charges Q_{it} was constructed geometrically. Using the Gaussian Model simulations for n- and p-type silicon based on the two sets of equations, belonging to exact and closed-form approximation solutions, were performed. Finally, using the D_{it} constant model, the strong dependence between the HF-CV curve slope and the D_{it} was verified.

Analysis and comparison of experimental and simulated HF-CV curves

The validation of the simulated HF-CV curves for different simulated passivation parameters through experimental data was the key part of this work. For this purpose, experimental data of a thermally grown SiO_2 layer with a thickness of 100 nm on n-type c-Si was taken into account. Thermally grown SiO_2 is considered a suitable material as an experimental reference because of its charge stability, as well as good insulating and passivation properties. The experimental data comprised HF-CV curves, transient capacitance-time (C-t) curves and ΔC-V curves (constructed from the C-t curves). The last two ones were used in order to verify the reliability of the HF-CV curves.

Since the simulated HF-CV curves present some deviations in comparison with the calculated HF-CV curve by the extraction program, a correction algorithm of these deviations (modelling error) based on the comparison of these ideal curves is presented and used for the results.

The Gaussian, U-shape, and constant function models for the D_{it} were used in order to simulate the D_{it}. A first approach was the comparison of the HF-CV curves produced by these D_{it} models with the experimental HF-CV curve. The

HF-CV curve associated with the Gaussian model presented the best approximation resulting in the least simulation error. The shortest relative error is found for this curve in comparison with the others. The contribution of different defects functions of the Gaussian model on the HF-CV curve was discussed. The exponential functions $U_{T,c}$ and $U_{T,v}$ affect the curve in accumulation and inversion, respectively and the Gaussian distributions contribute with a better fit in depletion.

The HF-CV curve associated with the single state D_{it} model presented the largest relative error. Therefore, the representation of the D_{it} by the value at the midgap is not a suitable method for simulating a D_{it} for a HF-CV curve.

Extraction of an approximated D_{it} based on the U-shape model through simulated HF-CV curves

The U-shape model is supported on the previous results in order to obtain a fit of the simulated HF-CV curves. Therefore, the exponential functions were used to obtain a better fit in accumulation and inversion, whereas the constant parameter D_{it}^0 contributes strongly to the slope as commented.

The parameter D_{it}^0 equals to the previously extracted D_{it} at the midgap resulted in a poor approximation of the experimental HF-CV curve. A non-conventional fitting method for the D_{it} was proposed. This method allows to extract an approximation of the D_{it} based on the U-shape model through simulated HF-CV curves.

A comparison of the found D_{it} and Q_{it} with the experimentally extracted ones by this non-conventional method was performed. An error of less than 0.4 % and 3 % for the D_{it} and the Q_{it} were found, respectively.

This alternative way to approximate a D_{it} allows to obtain a D_{it} distribution based on the lowest Means Squared Error (MSE) from the experimental HF-CV curve. This means if there are some deviations or fluctuations in the HF-CV curve, the method considers their average. This could be applied, for example, in order to extract a D_{it} for curves with other incorporated non-idealities, such as oxide charge instabilities.

Finally, the parameter D_{it}^0 was interpreted as the average of the D_{it} values around the midgap, where the recombination is largely significant, which could represent a

representative value of the D_{it} in comparison with the typical D_{it} value at midgap.

Outlook: HF-CV simulation tool enhancement

Since the HF-CV simulation tool was developed and evaluated based on a thermal SiO_2/c-Si MOS system, in order to extend the application scope, the respective constants of other passivating materials could be added. Also, the simulations developed in the framework of this thesis are based on the classical solution of the Poisson Equation which is sufficient for most passivating materials. However, in the industry, new passivating or dielectric materials in other fields are being developed and investigated, as well as new semiconductors, such as Si-Ge, germanium, III-V compound semiconductors with high-k dielectrics [Anw17]. Hence, an extension of this program could consider adding a quantum approach through quantum mechanical corrections or using the self-consisted solution of the Schrödinger and Poisson equations [Anw17].

The fitting method based on the U-shape model was performed using a relatively simple algorithm that comes from looking for an approximation of the minimum MSE of the simulated HF-CV curves. Further work in this part could include an optimization method for the non-linear systems in order to reduce the calculation time and using another D_{it} models, for example, the Gaussian model previously discussed.

Finally, a further investigation concerning the D_{it} models is needed in order to extract more information about the surface defect states for a given MOS system. The D_{it} models considered in this work are still relatively limited and just approximations of the "real" D_{it} since the models generally come from empirical considerations.

A: Publications

Publications in the frame of this thesis

- M. A. Sevillano, R. Grieseler, J. A. Guerra, J. A. Töfflinger. *Capacitance voltage curve simulations for different passivation parameters of dielectric layers on silicon.* Peruvian Workshop on Solar Energy (JOPES), 2019 in Lima, Peru, talk.

Other publications

- J. A. Dulanto, M. A. Sevillano , S. Espinoza, J. A. Guerra, R. Grieseler, J. A. Töfflinger. *Sputtered AlN:H passivation layers on crystalline silicon: Interface investigation of charge stability and defect states.* XVII Brazil MRS meeting, 2018 in Natal, Brazil, talk.

B: Acknowledgements

I would like to thank the National Council of Science, Technology and Technological Innovation (Concytec) from Peru for the award of a scholarship which made it possible to do this research work.

Thanks are also given to the Materials Science and Renewable Energy Group (MatER) of the Pontificia Universidad Católica del Perú (PUCP), for its support through the development of the research. I would also like to thank the Helmholtz Zentrum Berlin (HZB) from Germany for allowing me to do an internship, which allowed me to deepen my studies on physics of semiconductors, and for the production of the thermal SiO_2/c-Si MOS capacitor device, whose HF-CV measurements were studied in this thesis.

I must thank Dr. Amaru Töfflinger, my principal supervisor during the last two years. I am very indebted to Amaru for motivating my interest in photovoltaic research through lengthy discussions, inside and outside the university. Amaru's permanent guidance and confidence have been a key component to deepen into my studies freely and also for helping me to access the necessary tools, instruments, and equipment for the research.

Another large debt owed to Dr. Walter Füssel, who allowed me to visit him at home, on several occasions, to discuss different topics of semiconductor physics, especially about the capacitance-voltage (CV) technique, in addition, to providing me some of his personal notes to better understand this technique and achieve the objectives that were raised in this work.

I am very grateful to Dr. Andrés Guerra for his advice during the entire process of my Master's degree, as well as his constant guidance. I also have to thank Dr. Rolf Grieseler for his constant motivation in the research, and his total support in matters of Material Science. I also thank Dr. Lars Korte who received me in Berlin

during my stay and was very supportive of any eventuality. Special recognition I have to Dr. Thomas Dittrich from the HZB, who during two full months instruct me on semiconductor interface topics, and was willing to discuss different ideas and topics related to the HF- CV technique. I must also thank Dr. Klaus Lips from the Freie Universität Berlin (FU Berlin) for allowing me to attend his Photovoltaic lectures, each one of them was a complete inspiration to me, also for his advice and for solving some of my doubts. I also thank Dr. Daniel Amkreutz from PVcomB, with whom I was able to discuss very specific topics about the CV technique.

I am very grateful to Dr. Anibal Valera from the Universidad Nacional de Ingeniería (UNI), my supervisor during the undergraduate program, who was always willing to discuss the advances of my thesis. To Professor Robinson Vásquez from the UNI, who I admire his deep conceptual understanding in Physics, I appreciate all his advices in all areas, always so accurate at all the time. I thank Dr. Alex Dávila, with whom we enthusiastically spend several full evenings discussing topics of Physics, Psychology, and Computing. To Professor César Guerra, who helped me computationally, his advice on some algorithms was very important.

I also thank some other people with whom I could share different ideas about my research topic: Jorge Dulanto, Dr. Cham Trinh, Martina Thrams, Luis Conde, Luis Pretell, María del Carmen Mejía, Carlos Torres, Paul Llontop and especially to Álvaro Tejada, for all his support in the development of my studies.

Many thanks to Liz Montañez, who helped me unconditionally in my learning on the interpretation of interfacial phenomena in semiconductors.

I thank the management of Dr. Maria Elena López, director of the master's program, who was always present for any eventuality during the development of my studies.

Finally, I express deep gratitude to my friends and family, their company was always important.

References

[Abe00] Aberle, Armin G. "Surface passivation of crystalline silicon solar cells: a review". In*Progress in Photovoltaics: Research and Applications* 8.5 (2000), pp. 473–487. ISSN: 10627995. DOI: 10.1002/1099-159X(200009/10)8:5<473::AID-PIP337>3.0.CO;2-D (cit. on p. 17).

[Abe92] Aberle, Armin G., Glunz, Stefan, and Warta, Wilhelm. "Impact of illumination level and oxide parameters on Shockley-Read-Hall recombination at the Si-SiO2interface". In*Journal of Applied Physics* 71.9 (1992), pp. 4422–4431. ISSN: 00218979. DOI: 10.1063/1.350782 (cit. on p. 48).

[Anw17] Anwar, Sarkar R M et al. "Comprehensive Capacitance-Voltage Simulation and Extraction Tool Including Quantum Effects for High-k on Si x Ge 1-x and In x Ga 1-x As: Part I-Model Description and Validation". In*IEEE Transactions on Electron Devices* 64.9 (2017), pp. 3786–3793. ISSN: 0018-9383. DOI: 10.1109/TED.2017.2725645. URL: http://ieeexplore.ieee.org/document/7987802/ (cit. on pp. 13, 78).

[Arn98] Arns, R.G. "The other transistor: early history of the metal-oxide semiconductor field-effect transistor". In*Engineering Science & Education Journal* 7.5 (1998), pp. 233–240. ISSN: 0963-7346. DOI: 10.1049/esej:19980509. URL: https://digital-library.theiet.org/content/journals/10.1049/esej{_}19980509 (cit. on p. 15).

[Bla16] Black, Lachlan E. "New Perspectives on Surface Passivation: Understanding the Si-Al2O3 Interface". PhD thesis. 2016, pp. 15–29. ISBN: 978-3-319-32520-0. DOI: 10.1007/978-3-319-32521-7. URL: http://link.springer.com/10.1007/978-3-319-32521-7 (cit. on pp. 14, 16, 17, 27, 72).

[Bon17] Bonilla, Ruy S., Hoex, Bram, Hamer, Phillip, and Wilshaw, Peter R. "Dielectric surface passivation for silicon solar cells: A review". In*Physica Status Solidi (A) Applications and Materials Science* 214.7 (2017), p. 1700293. ISSN: 18626319. DOI: 10.1002/pssa.201700293. URL: http://doi.wiley.com/10.1002/pssa.201700293 (cit. on pp. 14, 16, 17, 48).

[Bra47] Brattain, W. H. and Shockley, W. "Density of Surface States on Silicon Deduced from Contact Potential Measurements". In*Physical Review* 72.4 (1947), pp. 345–345. ISSN: 0031-899X. DOI: 10.1103/PhysRev.72.345. URL: https://link.aps.org/doi/10.1103/PhysRev.72.345 (cit. on p. 16).

[Bre74] Brews, J. R. "An improved high-frequency MOS capacitance formula". In*Journal of Applied Physics* 45.3 (1974), pp. 1276–1279. ISSN: 00218979. DOI: 10.1063/1.1663401. URL: http://aip.scitation.org/doi/10.1063/1.1663401 (cit. on p. 38).

[Bro88] Brower, K. L. "Passivation of paramagnetic Si-SiO2 interface states with molecular hydrogen". In*Applied Physics Letters* 53.6 (1988), pp. 508–510. ISSN: 00036951. DOI: 10.1063/1.100620 (cit. on p. 43).

[Byr16] Byrnes, Steven J. *Maximum possible efficiency of a solar thermal energy system.* 2016. URL: http://sjbyrnes.com/ultimate{_}PV.html (cit. on p. 14).

[Cam02] Campbell, J. P. and Lenahan, P. M. "Density of states of Pb1 Si/SiO2 interface trap centers". In*Applied Physics Letters* 80.11 (2002), pp. 1945–1947. ISSN: 00036951. DOI: 10.1063/1.1461053 (cit. on p. 43).

[Cue15] Cuevas, Andres, Allen, Thomas, and Bullock, James. "Skin care for healthy silicon solar cells". In*2015 IEEE 42nd Photovoltaic Specialist Conference (PVSC)* 1 (2015), pp. 1–6. DOI: 10.1109/PVSC.2015.7356379. URL: http://ieeexplore.ieee.org/lpdocs/epic03/wrapper.htm?arnumber=7356379 (cit. on pp. 14, 18).

[Dev18] Devised, I S, For, Intended, Assessment, Technology, Without, I S, To, Regard, Considerations, Commercial, To, Pertaining, Products, Individual, and Equipment, O R. "the International Roadmap for Devices International Roadmap for Devices and Systems 2017 Edition Outside System Connectivity the Irds Is Devised and Intended for Technology Assessment Only and Is Without Regard To Any the International Roadmap for De-

vices". In (2018). URL: https://irds.ieee.org/images/files/pdf/2017/2017IRDS{_}OSC.pdf (cit. on p. 13).

[Din12] Dingemans, G. and Kessels, W. M. M. "Status and prospects of Al2O3-based surface passivation schemes for silicon solar cells". In *Journal of Vacuum Science & Technology A: Vacuum, Surfaces, and Films* 30.4 (2012), p. 040802. ISSN: 0734-2101. DOI: 10.1116/1.4728205. URL: http://avs.scitation.org/doi/10.1116/1.4728205 (cit. on p. 14).

[Dit10] Dittrich, Thomas. "Principle of Surface Photovoltage (SPV) Techniques and Applications on Solar Cell Materials". In (2010). URL: https://www.helmholtz-berlin.de/media/media/forschung/energie/heterogen/eta/methods/spv-techniques-2010-08-09.pdf (cit. on p. 18).

[Ent07] Entner, Robert. "Modeling and Simulation of Negative Bias Temperature Instability". PhD thesis. 2007. URL: http://www.iue.tuwien.ac.at/phd/entner/ (cit. on p. 42).

[Fen83] Fenske, F. "Simple improvement of the Lindner high-frequency MOS capacitance approximation". In *Physica Status Solidi (a)* 75.2 (1983), K141–K144. ISSN: 1521396X. DOI: 10.1002/pssa.2210750251. URL: http://doi.wiley.com/10.1002/pssa.2210750251 (cit. on pp. 34, 39, 54).

[Fey63] Feynman, Richard, Leighton, Robert B., and Sands, Matthew. *The Feynman Lectures on Physics*. Vol. 2. 6. Addison-Wesley Pub. Co, 1963, pp. 794–794 (cit. on p. 20).

[Fit68] Fitzgerald, D. J. and Grove, A. S. "Surface recombination in semiconductors (1967)". In *Surface Science* 9.July (1968), pp. 347–369 (cit. on p. 16).

[Fli95] Flietner, H. "Passivity and electronic properties of the silicon/silicondioxide interface". In *Materials Science Forum* 185-188.2 (1995), pp. 73–82. arXiv: 0402594 [cond-mat] (cit. on pp. 43, 67, 71).

[Fuc65] Fuchs, W. *Knaurs Buch der modernen Physik*. München Zürich: Droemersche Verlagsanstalt/für Bertelsmann Verlag, 1965, p. 359 (cit. on p. 20).

[Füs77] Füssel, Walter. "Ermittlung und Analyse von Termspektren Si/SiO2-Phasengrenze als Beitrag zur Klaerung der Natur der Zustaende". PhD. 1977 (cit. on pp. 28, 30, 31, 51, 60).

[Ger86] Gerardi, Gary J., Poindexter, Edward H., Caplan, Philip J., and Johnson, Noble M. "Interface traps and Pb centers in oxidized (100) silicon wafers". In*Applied Physics Letters* 49.6 (1986), pp. 348–350. ISSN: 00036951. DOI: 10.1063/1.97611 (cit. on p. 43).

[Gir88] Girisch, Reinhard B.M., Mertens, Robert P., and De Keersmaecker, Roger F. "Determination of Si-SiO2 Interface Recombination Parameters Using a Gate-Controlled Point-Junction Diode Under Illumination". In*IEEE Transactions on Electron Devices* 35.2 (1988), pp. 203–222. ISSN: 15579646. DOI: 10.1109/16.2441 (cit. on pp. 19, 48).

[Glu07] Glunz, S. W. "High-efficiency crystalline silicon solar cells". In*Advances in OptoElectronics* 2007.i (2007). ISSN: 1687563X. DOI: 10.1155/2007/97370 (cit. on pp. 14, 15).

[Gou07] Goudon, Thierry, Miljanovic, Vera, and Schmeiser, Christian. "On the Shockley-Read-Hall model: generation-recombination in semiconductors". In*Siam J. Appl. Math* 67.4 (2007), pp. 1183–1201 (cit. on p. 16).

[Gre19] Green, Martin A., Hishikawa, Yoshihiro, Dunlop, Ewan D., Levi, Dean H., Hohl-Ebinger, Jochen, Yoshita, Masahiro, and Ho-Baillie, Anita W.Y. "Solar cell efficiency tables (Version 53)". In*Progress in Photovoltaics: Research and Applications* 27.1 (2019), pp. 3–12. ISSN: 1099159X. DOI: 10.1002/pip.3102 (cit. on p. 14).

[Hau13] Haug, Halvard, Olaisen, Birger R., Nordseth, Ørnulf, and Marstein, Erik S. "A Graphical User Interface for Multivariable Analysis of Silicon Solar Cells Using Scripted PC1D Simulations". In*Energy Procedia* 38 (2013), pp. 72–79. ISSN: 18766102. DOI: 10.1016/j.egypro.2013.07.251. URL: https://linkinghub.elsevier.com/retrieve/pii/S1876610213013374 (cit. on pp. 18, 19).

[Hel94] Helms, C R and Poindexter, E H. "The silicon-silicon dioxide system: Its microstructure and imperfections". In*Reports on Progress in Physics* 57.8 (1994), pp. 791–852. ISSN: 0034-4885. DOI: 10.1088/0034-4885/57/8/002. URL: http://stacks.iop.org/0034-4885/57/i=8/a=002?key=crossref.4e17bd7aa3d9c674f9dfb33780aa5e2b (cit. on p. 43).

[Hen11] Henckel, Tim. "Intelligente Messwerterfassung der Hochfrequenz-Kapazitätskennlinie von Halbleiterstrukturen, deren Auswertung und grafischee Darstellung". Bacherlor Thesis. 2011 (cit. on pp. 28, 36, 51, 60).

[Int17] Intel. *Intel's 10 nm Technology: Delivering the Highest Logic Transistor Density in the Industry Through the Use of Hyper Scaling*. 2017. URL: https://newsroom.intel.com/newsroom/wp-content/uploads/sites/11/2017/09/10-nm-icf-fact-sheet.pdf (cit. on p. 13).

[KI92] Keithley-Instruments. *Model 230 programmable voltage source Instruction manual*. 1992. URL: https://www.equipnet.com/mp{_}data/media/5manual{_}2013911{_}17279{_}1.pdf (cit. on p. 28).

[KI99] Keithley-Instruments. *Model 590 CV analyzer Intruction manual (Revision D)*. 1999. URL: https://doc.xdevs.com/doc/Keithley/590/590{_}901{_}01D.pdf (cit. on pp. 28, 29).

[Kit57] Kittel, Charles and Fan, H. Y. "Introduction to Solid State Physics". In*American Journal of Physics* 25.5 (1957), pp. 330–330. ISSN: 0002-9505. DOI: 10.1119/1.1934457. URL: http://aapt.scitation.org/doi/10.1119/1.1934457 (cit. on p. 24).

[Kru14] Krugel, Georg, Jenkner, Franziska, Moldovan, Anamaria, Wolke, Winfried, Rentsch, Jochen, and Preu, Ralf. "Investigations on the passivation mechanism of AlN:H and AlN:H-SiN:H stacks". In*Energy Procedia* 55 (2014), pp. 797–804. ISSN: 18766102. DOI: 10.1016/j.egypro.2014.08.062. URL: http://dx.doi.org/10.1016/j.egypro.2014.08.062 (cit. on p. 14).

[Len98] Lenahan, P. M. and Conley, J. F. "What can electron paramagnetic resonance tell us about the Si/SiO2 system?" In*Journal of Vacuum Science & Technology B* 16.4 (1998), pp. 2134–2153. ISSN: 0734211X. DOI: 10.1116/1.590301 (cit. on p. 43).

[Li19] Li, Pei, Song, Yu, and Zuo, Xu. "Computational Study on Interfaces and Interface Defects of Amorphous Silica and Silicon". In*Physica Status Solidi - Rapid Research Letters* 1800547 (2019), pp. 1–21. ISSN: 18626270. DOI: 10.1002/pssr.201800547 (cit. on p. 43).

[Lin62] Lindner, R. "Semiconductor Surface Varactor". In*Bell System Technical Journal* 41.3 (1962), pp. 803–831. ISSN: 00058580. DOI: 10.1002/j.1538-7305.1962.tb00477.x. URL: http://ieeexplore.ieee.org/lpdocs/epic03/wrapper.htm?arnumber=6769600 (cit. on pp. 34, 38).

[Mat14] Matsudaira, Akira, Mehrotra, Saumitra Raj, Ahmed, Shaikh S., Klimeck, Gerhard, and Vasileska, Dragica. "MOSCap simulator [online]". In (2014). DOI: 10.4231/D3736M30D. URL: https://nanohub.org/resources/moscap (cit. on p. 15).

[McI14] McIntosh, Keith R. and Black, Lachlan E. "On effective surface recombination parameters". In*Journal of Applied Physics* 116.1 (2014). ISSN: 10897550. DOI: 10.1063/1.4886595 (cit. on p. 17).

[Mey47] Meyerhof, Walter E. "Contact Potential Difference in Silicon Crystal Rectifiers". In*Physical Review* 71.10 (1947), pp. 727–735. ISSN: 0031-899X. DOI: 10.1103/PhysRev.71.727. URL: https://link.aps.org/doi/10.1103/PhysRev.71.727 (cit. on p. 15).

[Mäc02] Mäckel, H. and Lüdemann, R. "Detailed study of the composition of hydrogenated SiNx layers for high-quality silicon surface passivation". In*Journal of Applied Physics* 92.5 (2002), pp. 2602–2609. ISSN: 0021-8979. DOI: 10.1063/1.1495529. URL: http://aip.scitation.org/doi/10.1063/1.1495529 (cit. on p. 14).

[Nic82] Nicollian, E. H. and Brews, J. R. "MOS (Metal Oxide Semiconductor) Physics and Technology". In (1982), pp. 1–3. ISSN: 00225355. DOI: 10.1116/1.571867 (cit. on pp. 18, 22, 24, 26, 31, 34, 38, 42, 46, 56, 60, 67).

[Nin19] Ning, Cun-Zheng. "Semiconductor nanolasers and the size-energy-efficiency challenge: a review". In*Advanced Photonics* 1.01 (2019), p. 1. ISSN: 2577-5421. DOI: 10.1117/1.AP.1.1.014002. URL: https://www.spiedigitallibrary.org/journals/advanced-photonics/volume-1/issue-01/014002/Semiconductor-nanolasers-and-the-size-energy-efficiency-challenge--a/10.1117/1.AP.1.1.014002.full (cit. on p. 13).

[Pie95] Pierret, R. F. *Semiconductor Device Fundamentals*. New York: Prentice Hall, 1995 (cit. on pp. 36, 38, 40, 60).

[Pie96] Pierret, Robert F. "Semiconductor Device Fundamentals". In*New York* (1996), p. 792. ISSN: 0342-1791. DOI: 10.1007/BF00198606. URL: http://books.google.com/books?id=GMZFHwAACAAJ{\&}pgis=1 (cit. on p. 26).

[Pop10] Pop, Eric. *Illinois ECE 440 Solid State Electronic Devices, Lecture 33: MOS Capacitance*. 2010. URL: https://nanohub.org/resources/8570 (cit. on p. 60).

[Pre07] Press, William H., Teukolsky, Saul A., Vetterling, William T., and Flannery, Brian P. *Numerical Recipes: The Art of Scientific Computing*. Cambridge University Press, 2007. ISBN: 9780521880688 (cit. on p. 40).

[Pre17] Preissler, Natalie. "Front-Side Interface Engineering for Liquid-Phase Crystallized Silicon Solar Cells on Glass". PhD thesis. 2017 (cit. on p. 51).

[Pur85] Purcell, E.M. *Electricity and Magnetism. Berkeley Physics Course. Vol. 2*. New York: McGraw-Hill, 1985 (cit. on p. 22).

[Rag99] Ragnarsson, Lars Ake and Lundgren, Per. "Electrical characterization of Pb centers in (100)Si-SiO2 structures: The influence of surface potential on passivation during post metallization anneal". In*Doktorsavhandlingar vid Chalmers Tekniska Hogskola* 938.1511 (1999), pp. 1–13. ISSN: 0346718X. DOI: 10.1063/1.373759 (cit. on p. 43).

[Rei18] Reinhardt, Karen and Kern, Werner. *Handbook of semiconductor wafer cleaning technology. 1993*. Andrew William, 2018. ISBN: 9780323510851 (cit. on p. 27).

[Ric01] Richter, C. A., Hefner, A. R., and Vogel, E. M. "Comparison of quantum-mechanical capacitance-voltage simulators". In*IEEE Electron Device Letters* 22.1 (2001), pp. 35–37. ISSN: 07413106. DOI: 10.1109/55.892436 (cit. on p. 15).

[Ric13] Richter, A., Hermle, M., and Glunz, S.W. "Crystalline Silicon Solar Cells Reassessment of the Limiting Efficiency for Crystalline Silicon Solar Cells". In*IEEE Journal of Photovoltaics* 3.4 (2013), pp. 1184–1191. DOI: 10.1109/JPHOTOV.2013.2270351 (cit. on p. 14).

[SO19] Stack-Overflow. *Stack Overflow's annual Developer Survey*. 2019. URL: https://insights.stackoverflow.com/survey/2019 (cit. on p. 33).

[Sch09] Schroder, Dieter K. "Electrical Characterization of Defects in High-k Gate Dielectrics". In*2005 International Semiconductor Device Research Symposium* (2009), pp. 209–210. DOI: https://doi.org/10.1201/9781420043778.ch5 (cit. on pp. 18, 41).

[Sho39] Shockley, William. "On the Surface States Associated with a Periodic Potential". In*Physical Review* 56.4 (1939), pp. 317–323. ISSN: 0031-899X. DOI: 10.1103/PhysRev.56.317. URL: https://link.aps.org/doi/10.1103/PhysRev.56.317 (cit. on p. 15).

[Sho48] Shockley, W. and Pearson, G. L. "Modulation of Conductance of Thin Films of Semiconductors by Surface Charges". In*Physical Review* 74.2 (1948), pp. 232–233. ISSN: 0031-899X. DOI: 10.1103/PhysRev.74.232. URL: https://link.aps.org/doi/10.1103/PhysRev.74.232 (cit. on p. 16).

[Sho52] Shockley, W. and Read, W. T. "Statistics of the Recombination of Holes and Electrons". In*Physical Review* 87.46 (1952), pp. 835–842. ISSN: 0031-899X. DOI: dx.doi.org/10.1103/PhysRev.87.835 (cit. on p. 16).

[Sho61] Shockley, William and Queisser, Hans J. "Detailed balance limit of efficiency of p-n junction solar cells". In*Journal of Applied Physics* 32.3 (1961), pp. 510–519. ISSN: 00218979. DOI: 10.1063/1.1736034. arXiv: 9809069v1 [arXiv:gr-qc] (cit. on p. 14).

[Sho63] Shockley, W. *Electrons and Holes in Semiconductors: With Applications to Transistor Electronics*. Bell Labor. Van Nostrand, 1963 (cit. on p. 33).

[Sou06] Southwick, Richard G. and Knowlton, William B. "Stacked dual-oxide MOS energy band diagram visual representation program (IRW student paper)". In*IEEE Transactions on Device and Materials Reliability* 6.2 (2006), pp. 136–145. ISSN: 15304388. DOI: 10.1109/TDMR.2006.876971 (cit. on pp. 19, 35, 55).

[Sta08] Stauffer, Lee. "C-V Measurement Tips , Tricks , and Traps". In*Keithley* 44139.December (2008) (cit. on p. 28).

[Sze07] Sze, S. M. and Ng, Kwok K. *Physics of Semiconductor Devices*. Hoboken, NJ, USA: John Wiley & Sons, Inc., 2007, pp. 1–649. ISBN: 9781493911516. DOI: 10.1007/978-1-4939-1151-6. arXiv: 9809069v1 [arXiv:gr-qc]. URL: http://doi.wiley.com/10.1002/0470068329 (cit. on pp. 26, 42, 44, 46).

[Tam32] Tamm, Ig. "Über eine mögliche Art der Elektronenbindung an Kristalloberflächen". In*Zeitschrift für Physik* 76.11-12 (1932), pp. 849–850. ISSN: 1434-6001. DOI: 10.1007/BF01341581. URL: http://link.springer.com/10.1007/BF01341581 (cit. on p. 15).

[Tar73] Tarasov, Lev Vasilevich and Tarasova, Aldina Nikolaevna. *Questions And Answers In School Physics*. Mir Publishers, 1973 (cit. on p. 22).

[Ter62] Terman, L. M. “An investigation of surface states at a silicon/silicon oxide interface employing metal-oxide-silicon diodes”. In*Solid State Electronics* 5.5 (1962), pp. 285–299. ISSN: 00381101. DOI: 10.1016/0038-1101(62)90111-9 (cit. on p. 31).

[Töf14] Töfflinger, Jan Amaru. “Interface investigations of passivating oxides and functional materials on crystalline silicon”. PhD thesis. 2014. URL: https://d-nb.info/1067387420/34 (cit. on pp. 43, 51, 52, 60).

[Vas08] Vasileska, Dragica. *MOS Capacitors: Theory and Modeling - Talk*. 2008. URL: https://nanohub.org/resources/5087 (cit. on p. 60).

[War99] Warner, R. M. and Grung, B. L. *MOSFET Theory and Design*. Oxford University Press, 1999, p. 272. ISBN: 10: 0195116429 (cit. on p. 41).

[Wer74] Werner, Wolfgang M. “The work function difference of the MOS-system with aluminium field plates and polycrystalline silicon field plates”. In*Solid State Electronics* 17.8 (1974), pp. 769–775. ISSN: 00381101. DOI: 10.1016/0038-1101(74)90023-9 (cit. on p. 40).

[Whi55] White, H. E. *Descriptive college physics*. New York: Van Nostrand, 1955 (cit. on p. 22).

[Xia14] Xiao, Shaoqing and Xu, Shuyan. “High-efficiency silicon solar cells - Materials and devices physics”. In*Critical Reviews in Solid State and Materials Sciences* 39.4 (2014), pp. 277–317. ISSN: 15476561. DOI: 10.1080/10408436.2013.834245 (cit. on p. 27).

[Yos17] Yoshikawa, Kunta et al. “Silicon heterojunction solar cell with interdigitated back contacts for a photoconversion efficiency over 26%”. In*Nature Energy* 2.5 (2017). ISSN: 20587546. DOI: 10.1038/nenergy.2017.32 (cit. on p. 14).